

Case Report

Distribution and Storage Characteristics of Soil Organic Carbon in Tidal Wetland of Dandou Sea, Guangxi

Mengsi Wang^{1,2,3}, Huanmei Yao^{1,2,3,*}, Zengshiqi Huang^{1,2,3}, Yin Liu^{1,2,3}, Meijun Chen^{1,2,3}, Maoyuan Zhong^{1,2,3} and Junchao Qiao^{1,2,3}

¹ College of Resources, Environment and Materials, Guangxi University, Nanning 530004, China; 2115303024@st.gxu.edu.cn (M.W.); 2115392020@st.gxu.edu.cn (Z.H.); 2115392051@st.gxu.edu.cn (Y.L.); 2215393003@st.gxu.edu.cn (M.C.); 2215393096@st.gxu.edu.cn (M.Z.); 2215393053@st.gxu.edu.cn (J.Q.)

² Key Laboratory of Environmental Protection, Education Department of Guangxi Zhuang Autonomous Region, Guangxi University, Nanning 530004, China

³ Guangxi Key Laboratory of Emerging Contaminants Monitoring, Early Warning and Environmental Health Risk Assessment, Nanning 530004, China

* Correspondence: yaohuanmei@gxu.edu.cn; Tel.: +86-13481105472

Abstract: In order to study the distribution characteristics of soil organic carbon (SOC) and soil organic carbon storage (SOCS) among different wetland types in Dandou Sea tidal wetland in Guangxi, firstly, based on Sentinel-2 imaging and random forest algorithm, combined with the existing tidal wetland data, a 10 m resolution tidal wetland dataset in Guangxi from 2019 to 2023 was generated, covering mangroves, salt marshes and tidal flats. The results show that the overall accuracy of the recognition results is higher than 96%, and the Kappa coefficient is higher than 0.95, which indicates high accuracy. Subsequently, the distribution characteristics and influencing factors of SOC and SOCS in different habitats were analyzed. The results showed that the SOC content of mangroves and salt marshes was higher than that of tidal flats. The SOC content of mangrove, salt marshes and tidal flats in 0–60 cm soil layer was 5.30–10.42 g/kg, 7.60–9.84 g/kg, and 1.29–2.25 g/kg, respectively. The changes of SOCS were 12.41–26.48 t/ha, 19.58–24.15 t/ha, and 3.61–6.86 t/ha, respectively. With the increase of soil depth, the SOC and SOCS of mangroves decreased gradually, and the SOC and SOCS of salt marshes increased gradually, and SOC and SOCS were mainly affected by soil bulk density (BD), soil moisture content (MC) and pH.

Keywords: tidal wetlands; Sentinel-2 imagery; soil organic carbon; Dandou Sea



Citation: Wang, M.; Yao, H.; Huang, Z.; Liu, Y.; Chen, M.; Zhong, M.; Qiao, J. Distribution and Storage Characteristics of Soil Organic Carbon in Tidal Wetland of Dandou Sea, Guangxi. *Atmosphere* **2024**, *15*, 431. <https://doi.org/10.3390/atmos15040431>

Academic Editors: Songlin Liu and Muhammad Ibrahim

Received: 1 March 2024

Revised: 21 March 2024

Accepted: 28 March 2024

Published: 30 March 2024



Copyright: © 2024 by the authors. Licensee MDPI, Basel, Switzerland. This article is an open access article distributed under the terms and conditions of the Creative Commons Attribution (CC BY) license (<https://creativecommons.org/licenses/by/4.0/>).

1. Introduction

The coastal zone is the interface between land and sea, possessing unique marine and terrestrial characteristics, and constitutes a dynamic and complex natural system [1,2]. Coastal wetlands, especially, hold a crucial position in addressing global climate change [3]. According to the definition of the Ramsar Convention, coastal wetlands extend from 6 m below sea level (often extending to the outer edge of large seaweed growth areas) to areas above the high tide line connected to freshwater or brackish lakes and marshes in the hinterland, as well as river sections upstream of seawater ingress [4]. Based on data from the United Nations Environment Programme (UNEP), the global area of coastal wetlands is approximately 34 million hectares, accounting for only about 3% to 5% of the world's land area, yet around 12% of the world's soil organic carbon (SOC) is stored in wetlands [5–8]. Therefore, wetlands play a crucial role in regulating the global carbon balance of terrestrial ecosystems [9–11].

There are many factors influencing SOC in wetlands, such as soil physicochemical properties [12,13], hydrological conditions [14], microbial types [15], and biophysical factors like climate [16,17]. However, SOC in wetlands is also influenced by different wetland types. For example, the study by Ji et al. [18] indicated that different land use types in

wetlands with varying vegetation cover significantly affect the concentration, distribution, and chemical structure of organic carbon in different density and particle size fractions. Vaughn et al. [19] investigated the organic carbon content in mangroves, salt marshes, and mixed areas of mangroves and salt marshes in northern Florida. The results showed that the organic carbon content in the mixed vegetation of mangroves and salt marshes is higher than in the adjacent areas of mangroves and salt marshes. Different geomorphological conditions also affect the content of SOC in wetlands. By comparing the non-degraded and degraded marine and estuarine mangroves within the Indonesian archipelago, Weiss et al. [20] concluded that the SOC content in natural marine mangroves is much higher than that in estuarine mangroves. De Jong Cleyndert et al. [21] explored the effect of ocean distance on the SOC content of mangroves in Lindi, Tanzania. The results showed that SOC was significantly negatively correlated with ocean distance, and SOC content decreased with the increase of distance from the sea. However, this is different from the results of the study in Micronesia, where the SOC is greater with the distance from the sea, which is mainly due to the deeper soil depth [22]. Donato et al. [23] found that in the estuaries and marine mangroves of the Indo-Pacific region, SOC did not change with the increase of distance from the sea, which may be due to the fact that all the samples were within 200 m from the edge of the ocean. It can be seen that soil erosion and soil depth are also important factors affecting SOC. In addition to common soil physical and chemical factors such as soil bulk density (BD), pH, and electrical conductivity (EC), salinity may also be a factor affecting wetland SOC. By using ultrapure water and artificial seawater to sequentially extract the soluble organic matter (WEOM) in mangrove soil, Kida et al. [24] proposed that high salinity may be one of the mechanisms leading to SOC accumulation in mangrove soil. However, Weiss et al. [20] pointed out that salinity did not affect SOC content. Whether salinity is a factor affecting wetland SOC remains to be further studied.

Additionally, changes in wetland types can lead to substantial variations in SOC within the same region. Sun et al. [25] investigated the changes in SOC under the invasion of *Spartina alterniflora* (*S. alterniflora*) in mangroves, revealing that the invasion increases the rate of SOC decomposition, thereby hindering its accumulation. Similarly, Wang et al. [26] examined SOC content changes during the afforestation of mangroves in tidal flats, demonstrating a significant increase in SOC content after the tidal flats evolved into mangroves. Ebrahim et al. [27] evaluated the impact of land use change on SOC caused by the conversion of mangroves into shrimp ponds. The results showed that the conversion of mangroves into shrimp ponds would lead to the loss of SOC reserves, which proved that human factors would lead to the reduction of SOC reserves, and human activities were also one of the factors affecting the SOC content of wetlands.

The current study mainly focuses on the SOC content of a single wetland category and its influencing factors, or the change of SOC when a certain wetland evolves into another wetland. For example, under different geomorphological conditions, the differences in organic carbon between mangrove ecosystems, as well as the effects of salinity, pH, soil texture [28] and other factors on SOC and soil organic carbon stock (SOCS). In addition, the impact of invasive species on SOC and SOCS in tidal wetlands is also a research focus. For example, the effects of *S. alterniflora* invasion of mangroves on SOC and SOCS. However, there are relatively few studies on the SOC content and SOCS characteristics of the whole tidal wetland, as well as the effects of various soil physical and chemical properties and related carbon components on the SOC and SOCS of the whole tidal wetland and the sub-categories of tidal wetland.

Therefore, in order to further explore the distribution characteristics of SOC in different wetland soils and their influencing factors, this study has utilized the Google Earth Engine (GEE) platform, combined with Sentinel-2 imagery and random forest algorithm, to generate higher-resolution classification data of Guangxi tidal wetlands. Based on this data, a spatial instead of temporal approach has been adopted to investigate the variations in SOC and SOCS content across different soil layers (0–20 cm, 20–40 cm, 40–60 cm) in the Dandou Sea and Tieshan Gulf areas of Guangxi. Additionally, the correlation between

SOC, SOCS, soil physicochemical properties, and other carbon components have been analyzed. This study not only fully understands the distribution characteristics of SOC in Guangxi tidal wetlands, but also finds the influence of different soil depth on SOC content. It has important theoretical value for further understanding the carbon storage of tidal wetlands and providing scientific basis and technical support for wetland protection and management.

2. Materials and Methods

2.1. Study Area

The coastal zone of Guangxi is located along the continental coastline within Guangxi territory ($107^{\circ}57' E$ – $109^{\circ}48' E$, $21^{\circ}00' N$ – $22^{\circ}15' N$), stretching from the Beilun River estuary at the China-Vietnam border in the west to the Ximi River estuary at the Guangxi-Guangdong border in the east, covering the administrative areas of Qinzhou, Beihai, and Fangchenggang. Major harbors include Qinzhou Bay, Fangchenggang Bay, Dafengjiang River Estuary Bay, Nanliujiang River Estuary Bay, Tieshan Bay, and Pearl Bay, among others. This study focuses on a 10-km buffer zone along the Guangxi coastline as the research area (see Figure 1), which is determined based on the definition of coastal wetlands. This research area includes three natural reserves: the Beilun River Estuary National Nature Reserve, the Maowei Sea Autonomous Region Nature Reserve, and the Shankuo National Nature Reserve. The coastline data are sourced from OpenStreetMap (OSM, <https://osmdata.openstreetmap.de/>, accessed on 2 August 2023).

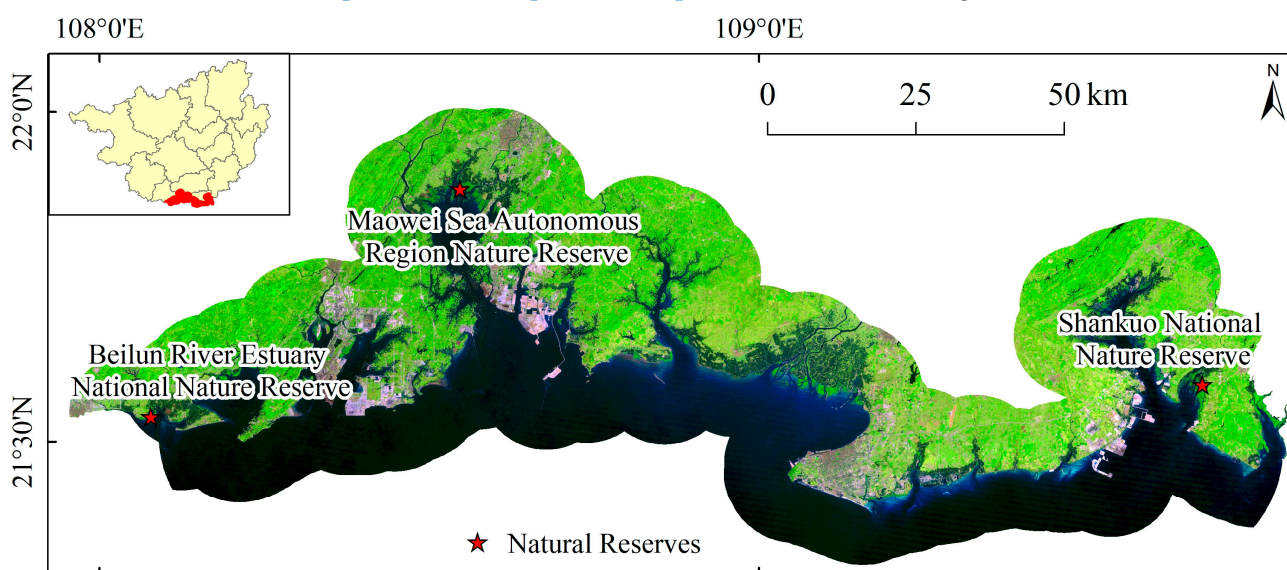


Figure 1. Illustration of the Study Area and Location of Natural Reserves (The yellow in the figure represents the administrative region of Guangxi, and the red represents the three natural reserves in Guangxi. In the base map, the Sentinel-2 satellite image is displayed as a true-color composite, with black areas representing water and green areas indicating vegetation).

2.2. Data Source

2.2.1. Sentinel-2 Data

The Sentinel-2 satellite is a high-resolution multispectral imaging satellite consisting of two polar-orbiting satellites (Sentinel-2A and -2B), equipped with a Multi-Spectral Instrument (MSI). It operates at an orbit height of 786 km and is primarily used for land monitoring. It provides image data covering aspects such as vegetation, soil, water coverage, inland waterways, and coastal areas, and can be utilized for emergency rescue services. Sentinel-2 offers publicly available multispectral images covering 13 discrete spectral bands ranging from 440 to 2200 nanometers. Its spatial resolutions are 10 m, 20 m, and 60 m, with a revisit period of 10 days for one satellite, complemented by two satellites, resulting

in a revisit period shortened to 5 days. This relatively high spatiotemporal resolution significantly increases the possibility of obtaining cloud-free images and detecting small tidal wetland patches under low/high tide conditions.

Through the GEE platform, users can directly access Sentinel-2 level-1C (L1C) and level-2A (L2A) data products. The Sentinel-2 data used in this study were L2A products, which mainly consist of atmospherically corrected surface reflectance data. The FMask algorithm [29] was applied to remove poor-quality observation pixels such as clouds, cloud shadows, and haze. Images from 2019 to 2023 with cloud cover of less than 70% were selected for the identification of tidal wetlands along the coastal areas of Guangxi. The Sentinel-2 image data used in the study are shown in Table 1. Table 2 lists the relevant parameters of the remote sensing images used.

Table 1. Sentinel-2 Image Data Used in the Study.

Year	Imaging Time Range	The Number of Available Images (Scenes)
2019	1 January 2019–31 December 2019	412
2020	1 January 2020–31 December 2020	451
2021	1 January 2021–31 December 2021	490
2022	1 January 2022–31 December 2022	363
2023	1 January 2023–31 December 2023	381

Table 2. Relevant Parameters of the Sentinel-2 Images Used in the Study.

Band Name	Wavelength (nm)	Spatial Resolution (m)
Blue	496.6	10
Green	560	10
Red	664.5	10
NIR	835.1	10
SWIR1	1613.7	20
SWIR2	2202.4	20

2.2.2. DEM Data

The ALOS World 3D-30 m (AW3D_30) [30–32], developed by the Japan Aerospace Exploration Agency (JAXA), is a global digital surface model (DSM). Its horizontal resolution is approximately 30 m, with a vertical accuracy of about 5 m. This dataset is obtained using the Panchromatic Remote-sensing Instrument for Stereo Mapping (PRISM), which is onboard the Advanced Land Observing Satellite (ALOS). In this study, we acquired AW3D_30 data from the GEE platform to calculate elevation, slope, and aspect, assisting in the identification of coastal tidal wetlands.

2.2.3. Existing Tidal Wetland Datasets

To ensure accurate and comprehensive sampling, this study combined the high accuracy of visual interpretation methods with the advantages of rapidly generating sample points using various existing wetland datasets, thus generating sample points with high confidence levels. Throughout the research process, a series of relevant tidal wetland datasets were collected, covering mangrove and salt marsh data with different spatial and temporal resolutions. Additionally, global 30-meter tidal flat data [33] from 1999 to 2019 were gathered, with a new global tidal flat dataset generated every three years, achieving an overall accuracy of approximately 85.4%. All these data products exhibit high accuracy. For instance, the GMW v3.0 [34] dataset has an accuracy ranging from 91.4% to 94.6%, while the accuracy of the spatial distribution data for Chinese *S. alterniflora* reaches 98.36%. The specific tidal wetland datasets used are listed in Table 3.

In addition to the tidal datasets, two land cover datasets, namely GLC_FCS30 [35] and GlobeLand30 [36], were collected. These land cover products were utilized to generate non-wetland sample points as supplementary data, aiming to reduce potential errors in the tidal wetland identification process and enhance the confidence level of the identification results.

Table 3. Relevant Tidal Wetland Datasets Used in the Study.

Dataset Name	Data Author	Type	Year	Resolution
World Atlas of Mangroves (WAM)	Spalding et al. [37]		2010	1:1,000,000
Global Mangrove Watch (GMW v3.0)	Bunting et al. [34]		1996–2020	30 m
A global biophysical typology of mangroves (GBTM)	Worthington et al. [38]	Mangrove	1996–2016	30 m
Global Mangrove Classification Products (GMCP)	Xiao et al. [39]		2018–2020	10 m
Global distribution of mangroves USGS (GDM_USGS)	Giri et al. [40]		2011	30 m
Spatial distribution of <i>S. alterniflora</i> in China	Mao et al. and Liu et al. [41–43]	Salt marsh	2015	30 m
Guangxi distribution of <i>S. alterniflora</i>	Huang [44]		2009–2020	30 m
Global distribution of tidal flat wetland ecosystems	Murray et al. [33]	Tidal flat	1999–2019	30 m

2.3. Collection of Sample Points and Determination of the Maximum Extent of Tidal Wetlands

2.3.1. Determination of Tidal Wetland Sample Points and Maximum Range

In this study, coastal tidal wetlands were divided into three categories: mangroves, salt marshes, and tidal flats. For mangrove sample points, to ensure their reliability, data from five mangrove datasets with different spatiotemporal resolutions were initially collected. Subsequently, by analyzing the temporal consistency of three mangrove datasets, namely GMW v3.0, GBTM, and GMCP, stable mangrove pixels were obtained. Then, the cross-consistency among these five mangrove datasets was analyzed, and pixels consistently identified as mangroves were selected as stable sample points. Finally, the spatial extent of these five mangrove datasets was combined to form the maximum mangrove range. The method for generating salt marsh sample points was similar to that for mangrove sample points. Firstly, the temporal consistency analysis was conducted on the Guangxi distribution of *S. alterniflora* data to obtain temporally stable salt marsh pixels. Secondly, the cross-consistency analysis of two salt marsh datasets was performed, and stable sample points for salt marshes were generated based on pixels consistently identified as salt marshes. This process is detailed in Equations (1) and (2).

$$\text{MaxExtent}_{\text{Mangrove}} = M_{\text{WAM}} \cup M_{\text{GMW}} \cup M_{\text{GBTM}} \cup M_{\text{GMCP}} \cup M_{\text{GDM_USGS}} \quad (1)$$

$$\text{MaxExtent}_{\text{Salt marsh}} = \cup_{t=2009}^{2020} \text{Guangxi } S. \text{ alterniflora}_t \cup \text{China } S. \text{ alterniflora} \quad (2)$$

where $\text{MaxExtent}_{\text{Mangrove}}$ represents the maximum extent of mangrove, which can serve as the boundary for mapping mangrove. M_{WAM} , M_{GMW} , M_{GBTM} , M_{GMCP} and $M_{\text{GDM_USGS}}$ are the spatial distributions of five global mangrove products listed in Table 3. $\text{MaxExtent}_{\text{Salt marsh}}$ represents the maximum extent of salt marsh, which can serve as the boundary for mapping salt marsh. $\text{Guangxi } S. \text{ alterniflora}_t$ and $\text{China } S. \text{ alterniflora}$ are the spatial distributions of two *S. alterniflora* products listed in Table 3, t represents the spatial distribution data of *S. alterniflora* in Guangxi in in year t , with t ranging from 2009 to 2020.

The tidal flat samples were collected using the 1999–2019 global tidal wetland data [33]. To ensure the accuracy of sample points, a temporal consistency analysis was conducted on the 1999–2019 global tidal wetland data, resulting in temporally stable tidal flat pixels, from which stable tidal flat sample points were generated. Additionally, the tidal flat data from 1999 to 2019 were combined to obtain the maximum tidal flat range. Furthermore, to ensure

the accuracy of tidal flat land class identification, a 10 km buffer zone was created along the coastline as the potential area for tidal flats. This process is detailed in Equation (3).

$$\text{MaxExtent}_{\text{Tidal flat}} = \begin{cases} \bigcup_{t=1999}^{2019} \text{Tidal flat}_t, \\ \text{Line}_{\text{coastal}} 10 \text{ km} \end{cases} \quad (3)$$

where $\text{MaxExtent}_{\text{Tidal flat}}$ represents the maximum extent of tidal flat, which can serve as the boundary for mapping tidal flat. Tidal flat is the spatial distribution of tidal flat products listed in Table 3, t denotes the tidal flat data in years, and the value range of t is 1999–2019. $\text{Line}_{\text{coastal}} 10 \text{ km}$ is a 10 km buffer zone towards the sea.

Finally, using high-resolution imagery from Google Earth and Sentinel-2 satellite data, a visual interpretation method was employed to compare and remove sample points that did not belong to their respective categories, resulting in stable sample points for tidal wetlands. Simultaneously, by combining the maximum extents of mangroves, salt marshes, and tidal flats, the largest possible area of tidal wetlands was generated, serving as the restricted zone for tidal wetland identification.

2.3.2. Obtaining Non-Wetland Stable Sample Points from Previous Land Cover Products

In the process of identifying tidal wetlands, collecting sample points of non-wetlands is essential in addition to sample points of tidal wetlands. This is because when generating the maximum tidal wetland extent, it is inevitable to include some non-wetland areas inland, and some non-wetland land cover types may have spectral similarities with tidal wetland land classes. Therefore, in addition to the sample points of the three types of tidal wetlands, sample points of five additional non-wetland land classes were also collected, including forests, croplands, grasslands, impervious surface, and water [45]. To automatically extract sample points of non-wetlands, this study collected two types of land cover data, GLC_FCS30 [35] and GlobeLand30 [36], and conducted time consistency and cross-consistency analyses on these two types of land cover data to extract stable sample points of the five non-wetland land classes, defining them as the ‘Other’ category.

Throughout the process of collecting sample points, 800 sample points each were generated for mangroves, salt marshes, and tidal flats, while 1500 sample points were collected for the ‘Other’ category.

2.4. Methods

2.4.1. Calculation of Spectral Indices

Before generating various water levels and phenological features, multiple spectral indices were calculated for each image in the dataset. These include Normalized Difference Vegetation Index (NDVI) [46], Modified Normalized Difference Water Index (mNDWI) [47], Normalized Water Difference Index (NDWI) [48], Land Surface Water Index (LSWI) [49], Enhanced Vegetation Index (EVI) [49], and Mangrove Vegetation Index (MVI) [50], with formulas as follows.

$$\text{NDVI} = \frac{\rho_{\text{NIR}} - \rho_{\text{Red}}}{\rho_{\text{NIR}} + \rho_{\text{Red}}} \quad (4)$$

$$\text{NDWI} = \frac{\rho_{\text{Green}} - \rho_{\text{NIR}}}{\rho_{\text{Green}} + \rho_{\text{NIR}}} \quad (5)$$

$$\text{mNDWI} = \frac{\rho_{\text{Green}} - \rho_{\text{SWIR1}}}{\rho_{\text{Green}} + \rho_{\text{SWIR1}}} \quad (6)$$

$$\text{LSWI} = \frac{\rho_{\text{NIR}} - \rho_{\text{SWIR1}}}{\rho_{\text{NIR}} + \rho_{\text{SWIR1}}} \quad (7)$$

$$\text{EVI} = 2.5 \times \frac{\rho_{\text{NIR}} - \rho_{\text{Red}}}{\rho_{\text{NIR}} + 6 \times \rho_{\text{Red}} - 7.5 \times \rho_{\text{Blue}} + 1} \quad (8)$$

$$\text{MVI} = \frac{\rho_{\text{NIR}} - \rho_{\text{Green}}}{\rho_{\text{SWIR1}} - \rho_{\text{Green}}} \quad (9)$$

where ρ_{Blue} , ρ_{Green} , ρ_{Red} , ρ_{NIR} and ρ_{SWIR1} represent the green, red, near-infrared, and shortwave infrared band 1 of the Sentinel-2 images, respectively.

2.4.2. Generation of Water Levels and Phenological Characteristics

The spectral characteristics of wetlands vary with seasonal or daily changes in water levels [40]. For example, during the rising tide in tidal wetlands, some wetland patches may be submerged, leading to misidentification as water pixels during the identification process. Therefore, to ensure the most comprehensive capture of submerged tidal wetland patches, it is necessary to generate composite images of the highest and lowest water levels when identifying tidal wetlands. Previous studies have shown that the NDVI of tidal flats is negatively correlated with tidal height, while the NDWI of tidal flats is positively correlated with tidal height [51]. Therefore, by using the “imageCollection.qualityMosaic()” function in the GEE platform with the maximum synthesis algorithm, maximum NDVI synthesis and maximum NDWI synthesis can be performed to generate images of the lowest and highest tides. Additionally, to better distinguish between vegetation and non-vegetation, water and non-water, this study also included the spectral values of Sentinel-2 images corresponding to the maximum NDVI and maximum NDWI in the spectral characteristics (e.g., Blue_NDVIMax, Blue_NDWIMax in Table 4), which were also used to calculate the six spectral indices mentioned above.

Table 4. Training Features of Tidal Wetlands.

Type	Features	Description	Number	Source
Spectrum	Blue, Green, Red, NIR, SWIR1, SWIR2, Blue_NDVIMax, Green_NDVIMax, Red_NDVIMax, NIR_NDVIMax, SWIR1_NDVIMax, SWIR2_NDVIMax, Blue_NDWIMax, Green_NDWIMax, Red_NDWIMax, NIR_NDWIMax, SWIR1_NDWIMax, SWIR2_NDWIMax	The 15th, 30th, 50th, 70th, and 85th percentile values for the 6 base bands of all images available during the study period, as well as the maximum NDVI and the maximum NDWI	42	Sentinel-2
Spectral Indices	NDVI, NDWI, mNDWI, LSWI, EVI, MVI, NDWI_NDVIMax, mNDWI_NDVIMax, LSWI_NDVIMax, EVI_NDVIMax, MVI_NDVIMax, NDVI_NDWIMax, mNDWI_NDWIMax, LSWI_NDWIMax, EVI_NDWIMax, MWI_NDVIMax	The 15th, 30th, 50th, 70th, and 85th percentiles of the 6 spectral indices for all images available during the study period, as well as the maximum NDVI and the maximum NDWI	40	Sentinel-2

Table 4. Cont.

Type	Features	Description	Number	Source
Temporal statistics	NDVI_StdDev, NDWI_StdDev, mNDWI_StdDev, LSWI_StdDev, EVI_StdDev, MVI_StdDev	Standard deviation of NDVI, NDWI, mNDWI, LSWI, EVI and MVI	6	Sentinel-2
Topography	Elevation, slope and aspect	Slope and aspect calculated from the AW3D_30 data	3	AW3D_30
Location	Longitude and latitude	Longitude and latitude for each pixel	2	N/A

Many studies have shown that multi-temporal phenological features help distinguish between vegetation wetlands and non-wetland land cover types [52,53]. Generally, there are two methods for acquiring vegetation phenological features, including seasonal compositing [35,54] and percentile-based compositing [35,55,56]. Azzari et al. [57] found that these two compositing methods have similar accuracy in land cover classification. Because percentile-based compositing considers the long-term trend of data, it helps analyze the variation of phenological features between different years. In contrast, seasonal compositing may overlook annual changes and may not be comprehensive enough when focusing on long-term trends. Considering the performance of both compositing methods, this study chose to use the percentile-based compositing method to generate phenological features, calculating the 5 percentile values (15th, 30th, 50th, 70th, and 85th) of the 6 basic bands (Blue, Green, Red, NIR, SWIR 1, and SWIR 2) and 6 spectral indices (NDVI, NDWI, mNDWI, LSWI, EVI, and MVI) in Sentinel-2 images. Additionally, considering the variation of spectral characteristics of different land cover types throughout the year, the standard deviation of the above 6 spectral indices was also calculated to further highlight phenological features.

Additionally, terrain variables are also important factors in determining the spatial distribution of wetlands [52]. Therefore, in this study, elevation, slope, and aspect calculated based on AW3D_30 data are considered as terrain features. In total, there are 93 features (listed in Table 4), including 88 optical features from Sentinel-2 images, 3 terrain features from AW3D_30 data, and 2 geographic coordinates.

2.4.3. Random Forest Algorithm

The conceptual basis of the Random Forest algorithm (RF) is the CART decision tree. It consists of multiple decision trees, and after training, determines the final classification result through a voting mechanism. Its core idea is to combine multiple weak classifiers into a strong classifier to improve overall classification or regression performance. Compared to other complex machine learning algorithms, Random Forest is relatively easy to implement and tune, and it has a certain level of robustness [58].

Therefore, in this study, the RF algorithm available on the GEE platform is used to identify tidal wetlands, as shown in Figure 2. To avoid overfitting, 70% of the sample points are randomly selected for training the RF classifier, while the remaining 30% are kept as test samples for evaluating the accuracy of the classification. The classification features inputted into the RF classifier are the water level and phenological features derived from the Sentinel-2 image collection (see Table 4). The number of decision trees in the RF classifier is set to 400, while other parameters remain at the default values provided by the GEE platform.

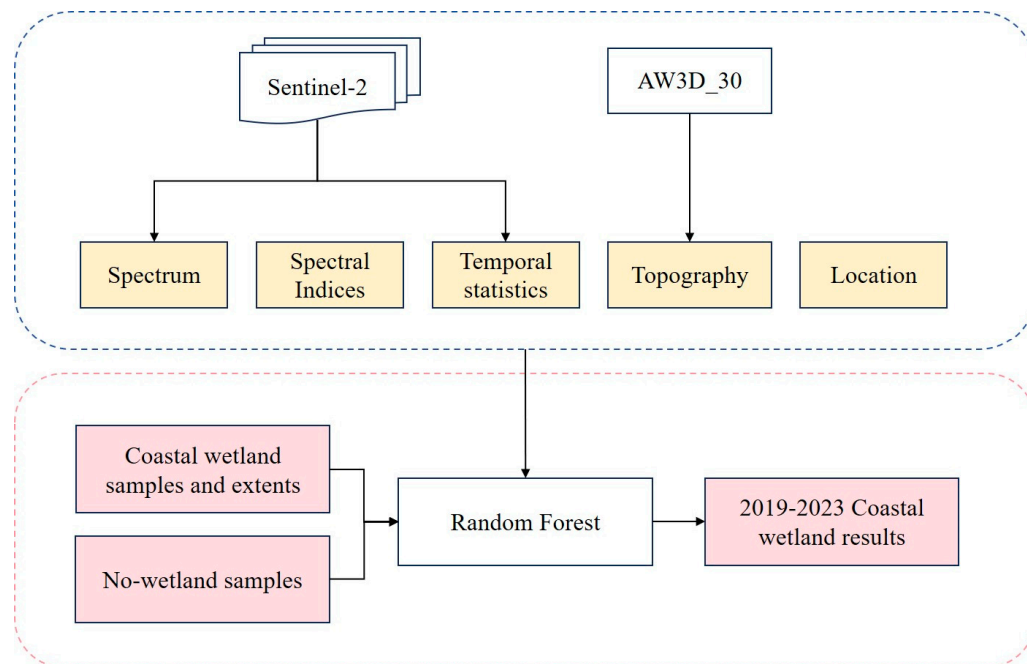


Figure 2. The Flowchart for Identifying Tidal Wetlands Using Water-Level, Phenology, Topography, and Geographic Location Features.

2.5. Sediment Sampling and Sample Treatment

Considering the accessibility constraints of field sampling, this study chose the Dandou Sea and Tieshan Gulf areas in Guangxi as the research area for soil organic carbon. Utilizing high-resolution imagery from Google Earth, Sentinel-2 image data, and the 2023 identification results of Guangxi tidal wetlands, sampling points were selected in the mangrove, tidal flat, and salt marsh areas of Dandou Sea and Tieshan Gulf based on random and equal principles. According to the ‘Technical Specifications for Soil Environmental Monitoring’, sediment samples at different depths were collected from 9 July 2023, to 12 July 2023. The specific distribution of sampling points is shown in Figure 3.

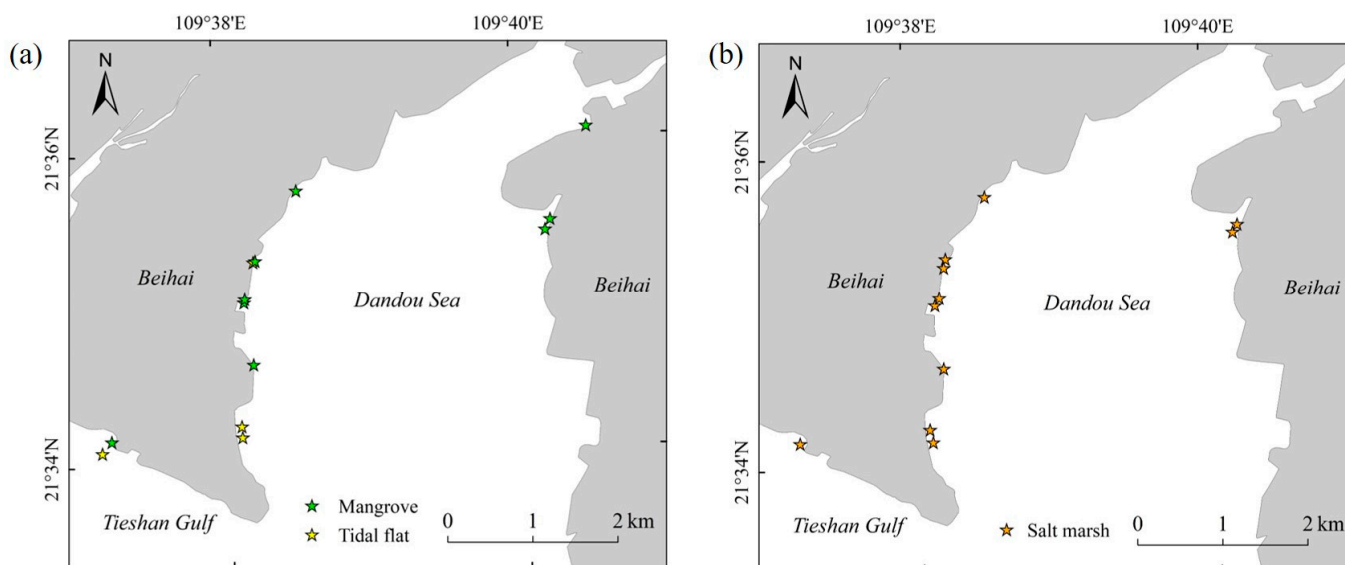


Figure 3. Geographical Locations of Field Sampling Points: (a) Tidal Flats and Mangroves, (b) Salt Marshes.

At these sampling points, there were 4 tidal flats, 9 mangroves, and 11 salt marshes, totaling 24 sampling points, each with a 0.25 m² quadrat established. Within each plot, a five-point sampling method was employed, and soil columns from depths of 0–60 cm were collected using a soil sampler, including samples from depths of 0–20 cm, 20–40 cm, and 40–60 cm. After removing soil impurities, the samples were placed in sealed polyethylene bags and transported to the laboratory immediately. Subsequently, the samples were dried in a cool, ventilated room, and various indicators such as SOC and soil physicochemical properties were determined. The methods for determining sediment physicochemical properties are shown in Table 5.

Table 5. Monitoring Methods for Sediment Soil Physicochemical Properties.

Monitoring Program	Analytical Method	Instrument	According to the Standard
pH	Potentiometry	pH-meter	HJ962-2018
MC	Gravimetric method	–	GB17378.5-2007
BD	Cutting-ring method	Cutting ring	NY/T1121.4-2006
EC	Conductivity meter method	Conductivity meter	F-HZ-DZ-DXS-0006

In addition, SOC content was determined using the potassium dichromate external heating oxidation method (NY/T 1121.6-2006, Ministry of Agriculture and Rural Affairs of China, 2006). Easily oxidizable organic carbon (EOC) was measured using the potassium permanganate method. Dissolved organic carbon (DOC) was measured by applying the same method used for SOC after the soil samples were centrifugally filtered.

2.6. Data Analysis

MC represents soil moisture content (%), with the formula:

$$MC = \frac{FW - DW}{FW} \times 100 \quad (10)$$

where FW denotes the soil fresh weight; DW denotes the soil dry weight.

BD represents soil bulk density (g/cm³), with the formula:

$$BD = g \times \frac{100}{v} \times (100 + MC) \quad (11)$$

where g denotes the fresh weight of ring knife soil (g); v denotes the ring knife volume (100 cm³).

SOCS represents soil organic carbon stock (t/ha), with the formula:

$$SOCS = \sum_i^n C_i \times BD_i \times E_i \times 0.1 \quad (12)$$

where C_i denotes carbon mass fraction in i soil depth (g/kg); BD_i denotes the soil BD in i soil depth (g/cm³); E_i denotes thickness of soil in i soil depth (cm); n denotes the number of soil depth layers.

The corresponding abbreviations and nomenclatures are shown in Tables A1 and A2.

3. Results

3.1. Accuracy Assessment

As shown in Table 6, the overall classification accuracy of tidal wetland identification results for five different years is above 96%, with Kappa coefficients all exceeding 0.95, indicating high accuracy of the identification results. In addition, this study calculated confusion matrices based on validation sample points and compiled the confusion matrices for the “mangroves”, “salt marshes”, “tidal flats”, and “other” categories for each year, while also computing the user accuracy (UA) and producer accuracy (PA) (see Tables A3–A7).

Table 6. Accuracy Assessment of Tidal Wetland Identification Results (2019–2023).

Year	2019	2020	2021	2022	2023
Overall accuracy (%)	96.88	98.63	97.66	96.31	98.86
Kappa	0.95	0.98	0.97	0.95	0.98

3.2. Spatial Pattern of Coastal Tidal Wetlands in Guangxi

The spatial distribution of tidal wetlands in Guangxi in 2023 is shown in Figure 4. The results indicate a specific pattern of spatial distribution of tidal wetlands in Guangxi. Within the study area, tidal flats are predominantly distributed along the coastline, with fewer occurrences near impermeable surfaces and more occurrences farther away from impermeable surfaces. Mangroves are primarily located in three natural reserves and near the Nanliu River basin, while the distribution of salt marshes is more scattered, mainly found near the Nanliu River basin, Tieshan Gulf, and the Dandou Sea area. The spatial distribution pattern of tidal wetlands from 2019 to 2022 is similar to that of 2023, as shown in Figure A1.

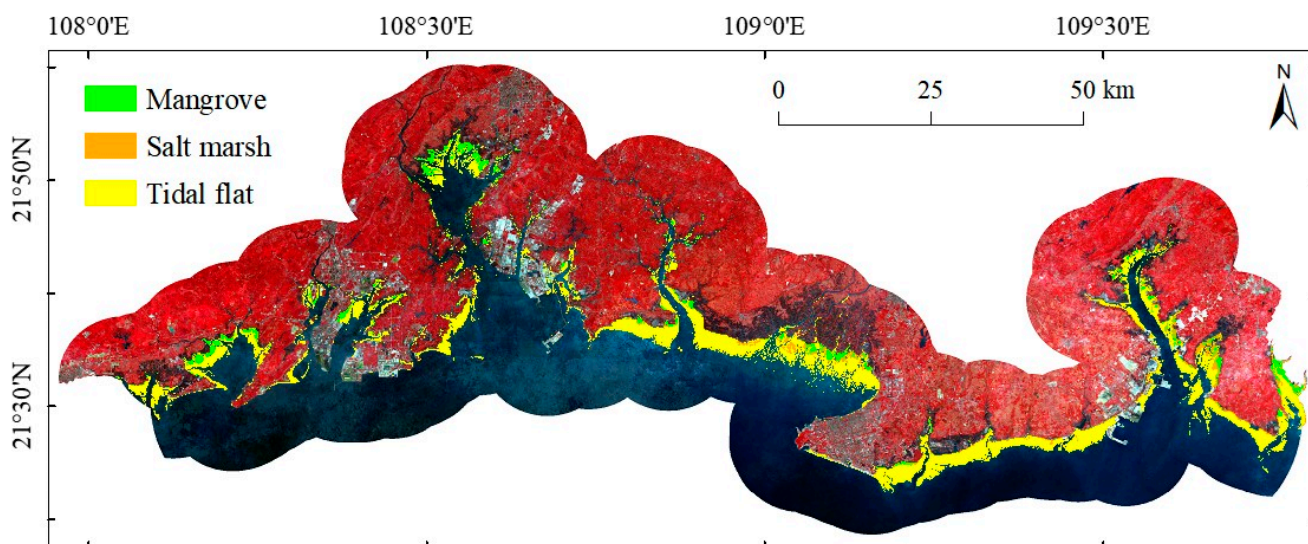


Figure 4. Spatial Distribution of Tidal Wetlands (Using 2023 as an Example. In the base map, the Sentinel-2 satellite image is displayed as a false-color composite, with black areas representing water and red areas indicating vegetation).

Quantitative statistics were conducted on the three categories of tidal wetlands to obtain the total area and percentage from 2019 to 2023, as detailed in Figure 5 and Table 7. Overall, in the coastal tidal wetlands of Guangxi, tidal flats account for the largest proportion, comprising approximately 80% of the total area, while mangroves account for around 15%, and salt marshes constitute the smallest proportion, at less than 10% of the total area. Regarding the trend of individual wetland categories from 2019 to 2023, mangrove wetlands had the largest proportion in 2023, reaching 7558.60 ha, and showed a gradual increase over the five-year period. The area of salt marsh wetlands generally increased first and then decreased, reaching its maximum in 2020 and subsequently decreasing each year. Meanwhile, the area of tidal flat wetlands remained relatively stable overall.

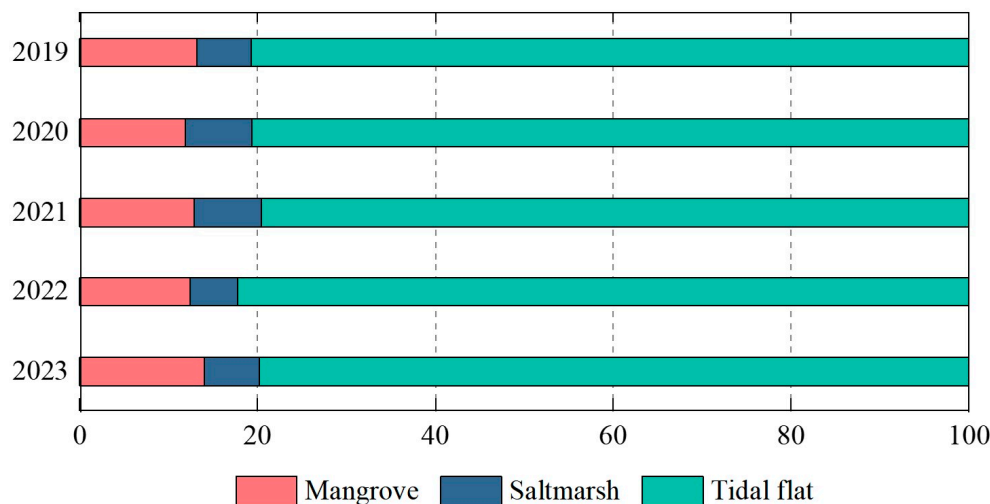


Figure 5. Proportional Area of the Three Wetland Categories from 2019 to 2023.

Table 7. Total Area of the Three Wetland Categories from 2019 to 2023.

	Mangrove (ha)	Salt Marsh (ha)	Tidal Flat (ha)	Total (ha)
2019	7274.41	3414.55	44,633.90	55,322.86
2020	6932.94	4429.53	47,232.70	58,595.17
2021	7322.94	4320.15	45,284.10	56,927.19
2022	7505.67	3234.21	49,829.60	60,569.48
2023	7558.60	3301.55	42,920.70	53,780.85

3.3. Distribution Characteristics of SOC in Different Habitat Types

SOC content varies significantly among the three different habitats in tidal wetlands, with notably higher levels observed under various vegetation covers compared to the tidal flats (see Figure 6). This indicated the significant impact of vegetation on SOC content in wetland soils. Additionally, there were significant differences in SOC content under different vegetation covers. Due to variations in vegetation types, development stages, and distribution patterns, each soil depth exhibited distinct characteristics in SOC content.

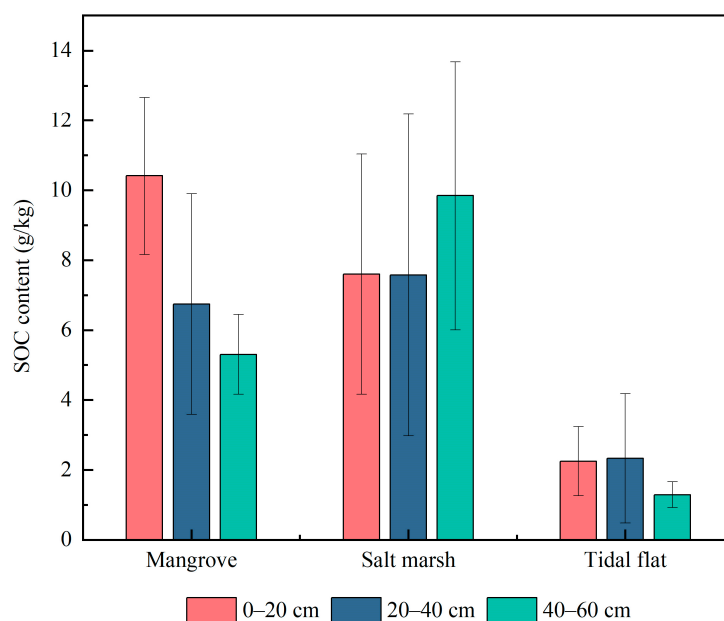


Figure 6. The Content of SOC in Three Different Habitats (Tidal Flats, Mangroves, and Salt Marshes).

From a vertical distribution perspective, the SOC content beneath the sampling points in mangrove wetlands was highest in the surface layer (0–20 cm), at 10.42 g/kg, which was approximately twice that of the deeper layer (40–60 cm); the SOC content fluctuates less in the depth range of 20–60 cm, with an average of 6.02 g/kg. In salt marsh wetlands, the SOC content varies little between the 0–20 cm and 20–40 cm soil depths, while in the soil at a depth of 40–60 cm, the organic carbon content could reach 9.84 g/kg. This may be due to the presence of long-standing salt marsh wetlands in the sampling area, which have relatively stable natural conditions, and as the years of growth increase, there was a clear trend of organic carbon accumulation. In contrast, the SOC content in tidal flats was lower across different soil depths. In the depths of 0–20 cm and 20–40 cm, the organic carbon content was relatively similar, while in the 40–60 cm layer, the organic carbon content decreases. This may be due to the influence of tidal fluctuations, which are not conducive to the accumulation of organic carbon.

3.4. Characteristics of SOCS in Different Habitat Types

The SOCS in different habitat types are illustrated in Figure 7. The results indicated that in the surface soil, the SOCS in mangrove wetlands was the highest, reaching up to 26.48 t/ha. However, with increasing soil depth, the SOCS in mangroves gradually decreases. By the depth of 40–60 cm, its content decreases to about half of that in the surface soil.

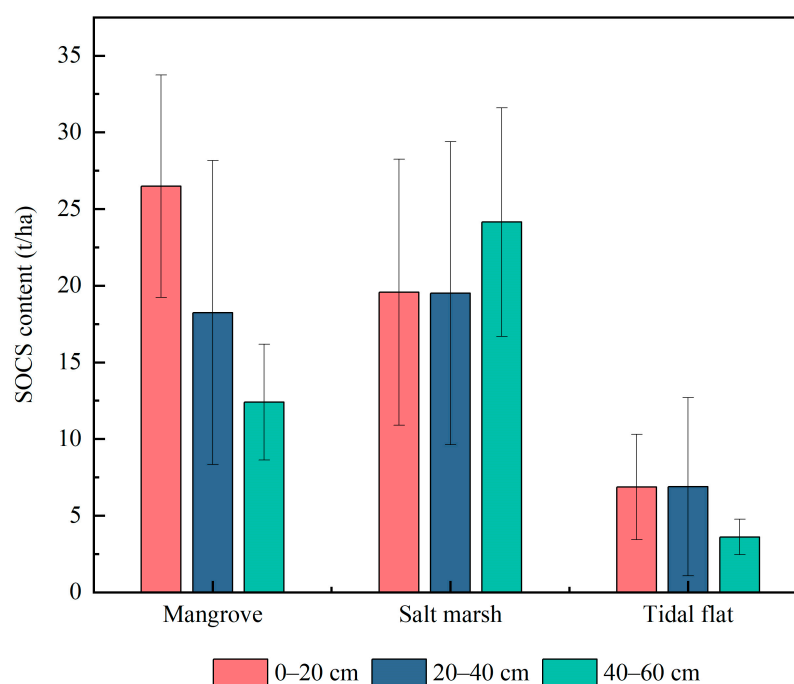


Figure 7. The Content of SOCS in Three Different Habitats (Tidal Flats, Mangroves, and Salt Marshes).

In salt marsh wetlands, the SOCS remained relatively stable at depths of 0–20 cm and 20–40 cm, but showed an increasing trend at a depth of 40–60 cm, reaching twice the SOCS level of mangroves at a depth of 40–60 cm. Compared to mangroves and salt marshes, the SOCS in tidal flat wetlands was lower. There was little difference in SOCS at depths of 0–20 cm and 20–40 cm, but a decreasing trend was observed at a depth of 40–60 cm.

3.5. Correlation between SOCS, SOC, Their Components, and Various Factors

The soil physicochemical properties and carbon components of mangroves, salt marshes, and tidal flats are shown in Table 8. The correlation between soil physicochemical properties of tidal wetlands and SOC, SOCS is shown in Table 9. The results indicated that SOC was positively correlated with MC, SOCS, EOC, and POC, and negatively correlated

with BD and pH. SOCS was positively correlated with MC, SOC, EOC, POC, and DOC, and negatively correlated with BD and pH.

Table 8. Soil Physicochemical Properties and Carbon Components of Different Habitat Types (Mean ± Standard Deviation).

Type	Sediment Depth (cm)	BD (g/cm ³)	MC (%)	pH	EC (µs/cm)	SOC (g/kg)	EOC (g/kg)	POC (g/kg)	DOC (g/kg)	SOCS (t/ha)
Mangrove	0–20 cm	1.26 ± 0.13	42.16 ± 9.26	6.32 ± 0.55	3.04 ± 0.48	10.42 ± 2.40	2.13 ± 1	7.76 ± 1.26	0.21 ± 0.21	26.48 ± 7.25
	20–40 cm	1.31 ± 0.2	37.19 ± 12.2	5.33 ± 2.1	2.61 ± 1.1	6.47 ± 3.16	1.48 ± 0.89	5.26 ± 2.41	0.41 ± 0.72	18.24 ± 9.91
	40–60 cm	1.16 ± 0.18	48.04 ± 2.57	6.27 ± 0.19	2.58 ± 0.04	5.30 ± 1.14	1.6 ± 0.09	3.71 ± 1.06	0.07 ± 0.03	12.41 ± 3.77
Salt marsh	0–20 cm	1.29 ± 0.15	35.25 ± 11.68	6.26 ± 1.06	3.08 ± 0.44	7.60 ± 3.44	1.32 ± 0.96	6.28 ± 3.00	0.18 ± 0.13	19.58 ± 8.68
	20–40 cm	1.37 ± 0.21	33.36 ± 15.49	5.79 ± 1.44	3.09 ± 0.49	7.58 ± 4.60	1.52 ± 1.02	6.05 ± 3.75	0.13 ± 0.12	19.51 ± 9.88
	40–60 cm	1.28 ± 0.23	39.32 ± 15.58	5.57 ± 1.19	3.56 ± 0.91	9.84 ± 3.84	1.78 ± 1.05	8.06 ± 3.23	0.19 ± 0.12	24.15 ± 7.45
Tidal flat	0–20 cm	1.49 ± 0.11	26.97 ± 8.58	6.55 ± 0.62	2.99 ± 0.83	2.25 ± 0.99	0.33 ± 0.34	1.92 ± 0.66	0.08 ± 0.02	6.86 ± 3.44
	20–40 cm	1.56 ± 0.16	26.71 ± 4.31	7.01 ± 0.79	3.26 ± 0.42	2.33 ± 1.85	1.08 ± 0.62	3.39 ± 2.45	0.16 ± 0.09	6.89 ± 5.80
	40–60 cm	1.35 ± 0.02	31.63 ± 0.63	6.61 ± 0.21	3.33 ± 0.41	1.29 ± 0.37	0.14 ± 0.08	1.14 ± 0.45	0.04 ± 0.03	3.61 ± 1.16

Table 9. Correlation between SOC and its Active Components with Other Soil Physicochemical Properties.

	BD	MC	pH	EC	SOC	SOCS	EOC	POC	DOC
BD	1								
MC	−0.943 **	1							
pH	0.503 *	−0.436	1						
EC	0.350	−0.412	0.205	1					
SOC	−0.591 *	0.616 *	−0.637 *	0.034	1				
SOCS	−0.544 *	0.566 *	−0.658 *	0.011	0.995 **	1			
EOC	−0.559 *	0.705 *	−0.509 *	−0.172	0.894 **	0.884 **	1		
POC	−0.447	0.492	−0.594 *	0.142	0.976 **	0.978 **	0.89 **	1	
DOC	−0.115	0.155	−0.640 *	−0.298	0.467	0.538 *	0.499 *	0.520 *	1

** $p < 0.01$, * $p < 0.05$.

For individual habitat types, as shown in Tables A8–A10, SOC in mangrove wetlands was significantly positively correlated with EC, SOCS, EOC, and POC, while SOCS was significantly positively correlated with BD, EC, SOC, EOC, and POC. SOC and SOCS in salt marshes were significantly positively correlated with MC, EC, EOC, POC, and DOC, and negatively correlated with BD and pH, with a positive correlation between them. As for tidal flats, SOC and SOCS were significantly positively correlated with BD, EOC, POC, and DOC, and negatively correlated with MC and EC, with a positive correlation between them.

4. Discussion

4.1. Comparison with Other Tidal Wetland Data

To comprehensively understand the classification performance of tidal wetlands in this study, three existing tidal wetland datasets (GMW v3.0, GMCP, and Murray’s tidal flat) were selected for comparative analysis, as shown in Table 2. Figure 8 presents the classification results of mangroves in 2020 for three typical regions (Maowei Sea area, Nanliu River Basin, and Dandou Sea area) compared with GMW v3.0 and GMCP. Overall, there was good consistency among the three mangrove identification results. This is mainly because mangroves have distinct and strong vegetation reflectance characteristics, making them easier to identify compared to other wetlands [49]. Specifically, the mangrove area in the Maowei Sea area was significantly underestimated in GMW v3.0, which may be due to the identification method. GMW v3.0 was based on the GMW v2.5 [59], which was established in 2010 and mapped the potential change areas of mangroves by calculating the difference between the maximum and minimum scattering in HH and HV polarization directions for each pixel in potential change areas. The mangrove existence areas were determined by setting difference thresholds. However, the setting of difference thresholds was determined by visual interpretation based on reference sites worldwide, and due to the uneven distribution of reference sites globally, with only one site set in Asia, the

obtained threshold may not be fully applicable to the coastal areas of China, resulting in poor identification performance. GMCP showed the highest consistency with this study in the Maowei Sea area and Nanliu River area, but there was an omission of mangrove identification in the Dandou Sea area. However, overall, the use of high-resolution imagery can more accurately identify the spatial patterns of mangroves.

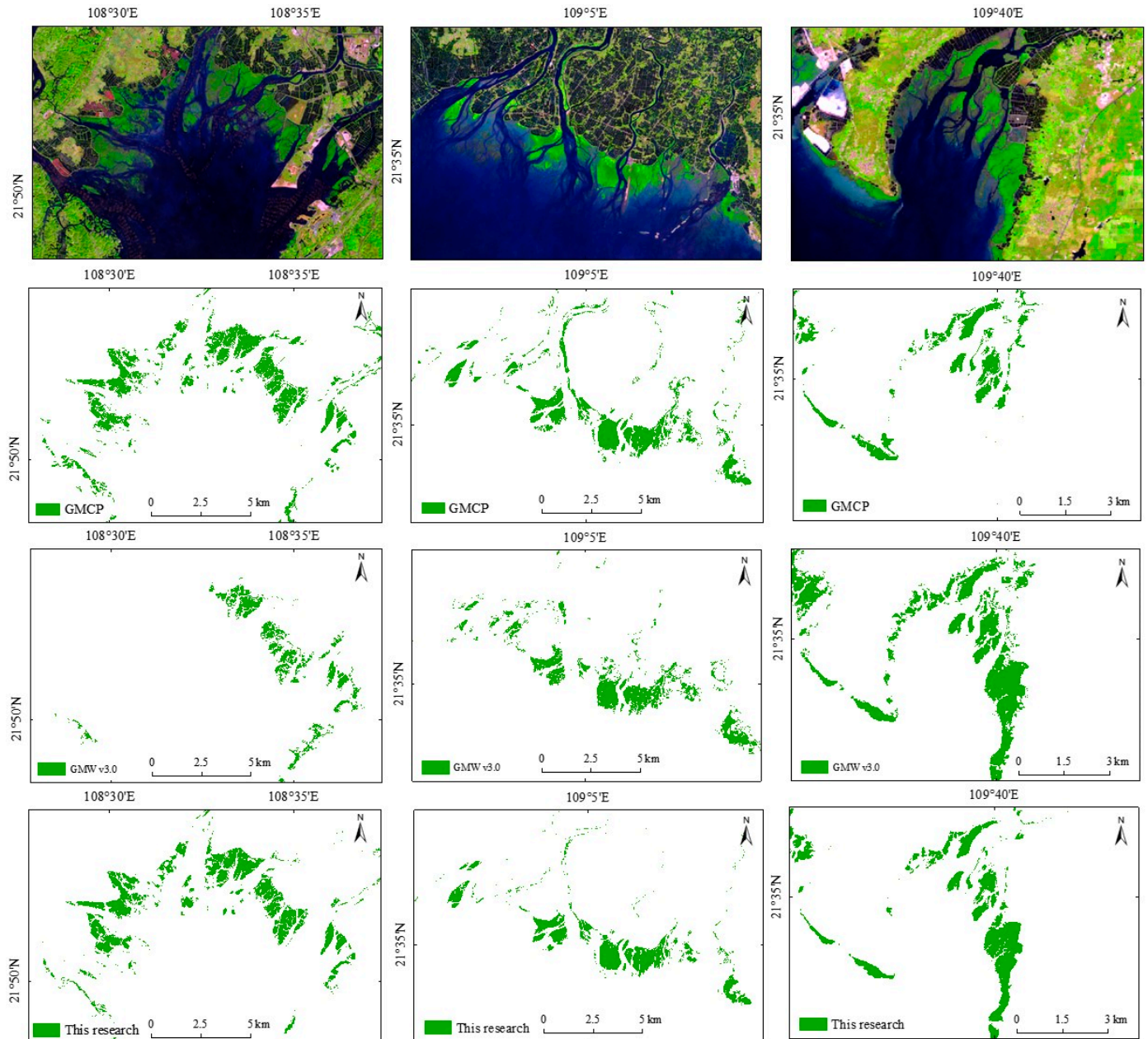


Figure 8. Cross-comparison of this study with two mangrove datasets (GMW v3.0 adapted with permission from Ref. [34], 2022, Bunting et al.; GMCP adapted with permission from Ref. [39], 2021, Xiao et al.).

Figure 9 shows the comparison between the tidal flats identified in this study and Murray's tidal flat V1.2 [33] from 2019, along with the corresponding minimum tide image of the area. Overall, both methods effectively captured the spatial pattern of tidal flats in the area with a high degree of consistency. However, comparing the original and minimum tide images with the identification results of Murray's tidal flat V1.2 revealed that some coastal aquaculture ponds are misidentified as tidal flats, whereas the tidal flat identification in this study successfully excludes these coastal aquaculture ponds. Additionally, in the Nanliu River area, Murray's tidal flat V1.2 misclassified a significant portion of salt marshes as tidal flats, while this study distinguished between salt marshes and tidal flats, as shown in Figure 10.

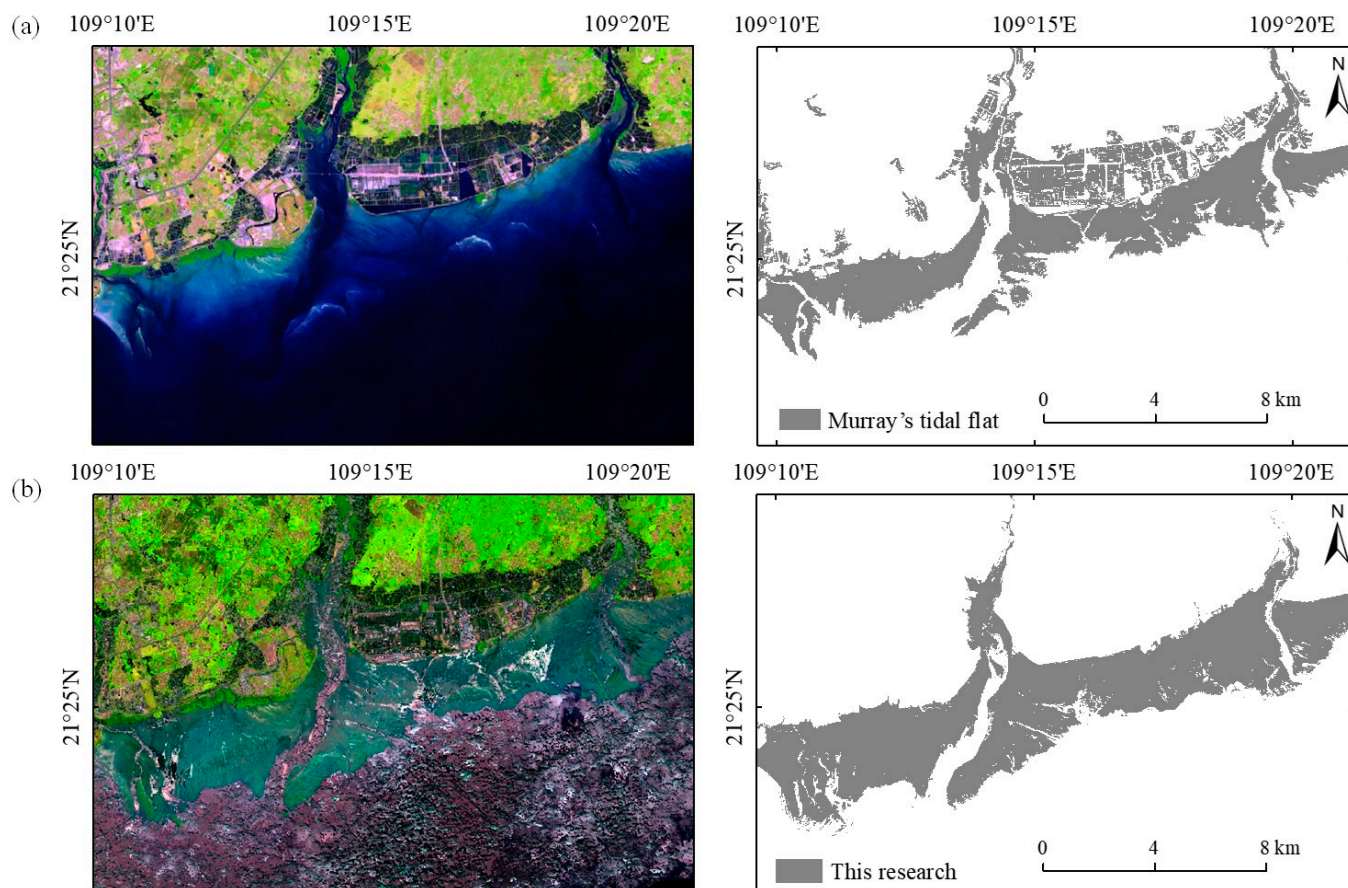


Figure 9. Comparison between the tidal flats identified in this study and Murray's tidal flat from 2019 (a) Original image, (b) Minimum tide image.

4.2. Differences in the Distribution of SOC and SOCS among Different Habitat Types

Overall, there were different trends in the SOC content among the three habitat types with increasing soil depth. Specifically, in mangrove wetlands, SOC gradually decreases with soil depth, while in salt marshes, SOC content increases with depth. Conversely, in tidal flats, SOC content remains relatively uniform across different soil depths. Previous studies have indicated that factors such as litter input, distribution pattern of plant roots, root exudates, and decomposition of root residues influence the distribution of SOC along soil profiles in different habitat types [60,61].

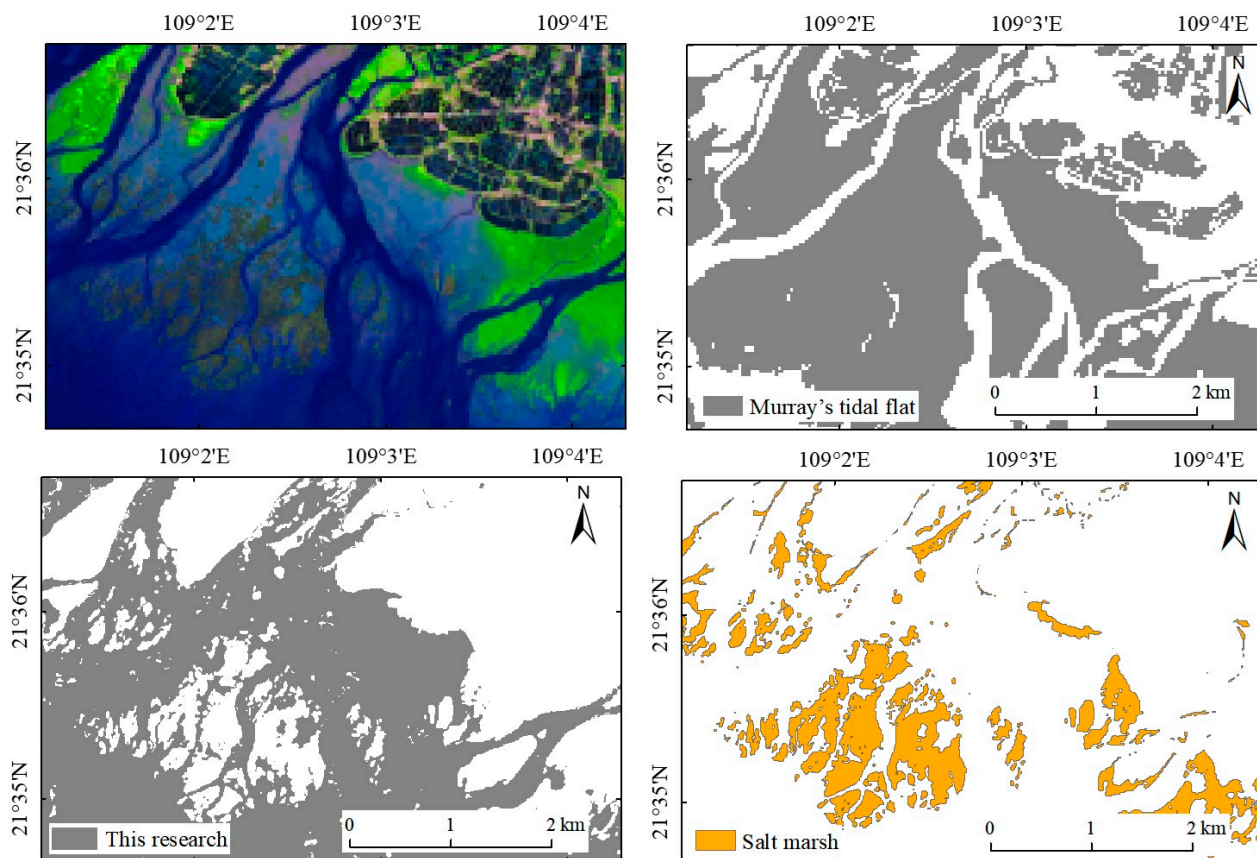


Figure 10. Comparison of tidal flats and salt marshes in the Nanliu River area with Murray's tidal flat.

As shown in Figure 11, in the surface soil layer (0–20 cm), the organic carbon content of each habitat type was as follows: mangroves > salt marshes > tidal flats. The highest organic carbon content is found in mangrove soil, primarily due to the high productivity and biomass accumulation capacity of mangrove ecosystems [19]. Mangroves can absorb large amounts of carbon dioxide through photosynthesis and convert it into organic matter, facilitating the accumulation of SOC. Moreover, mangroves are typically located in estuarine areas where terrestrial organic matter input, such as suspended solids and plant debris carried by rivers, enriches the surface SOC content [62]. In contrast, salt marshes have lower productivity than mangroves and are often located in tidal plains or estuaries, where surface soils are mainly influenced by seawater input. However, seawater generally contains lower organic matter content, resulting in lower SOC content in salt marshes compared to mangroves.

At depths of 20–40 cm and 40–60 cm, the organic carbon content of each habitat type was as follows: salt marshes > mangroves > tidal flats. Except for the surface soil layer, the organic carbon content in mangrove wetlands is lower than that in salt marshes. This may be because mangroves, as compared to salt marshes, are closer to inland areas and are submerged in tidal water for shorter periods, making organic carbon in surface soils more susceptible to oxidation. Salt marshes, on the other hand, are submerged in water for longer periods, resulting in prolonged anaerobic conditions that inhibit microbial activity and slow down organic matter decomposition [63]. This could lead to lower organic carbon content in mangroves than in salt marshes at depths of 20–40 cm and 40–60 cm. The organic carbon content in tidal flats is generally lower across all three depth layers, possibly due to their long-term inundation and frequent exposure to tidal flushing, which transports deposited organic carbon into the oceanic carbon pool.

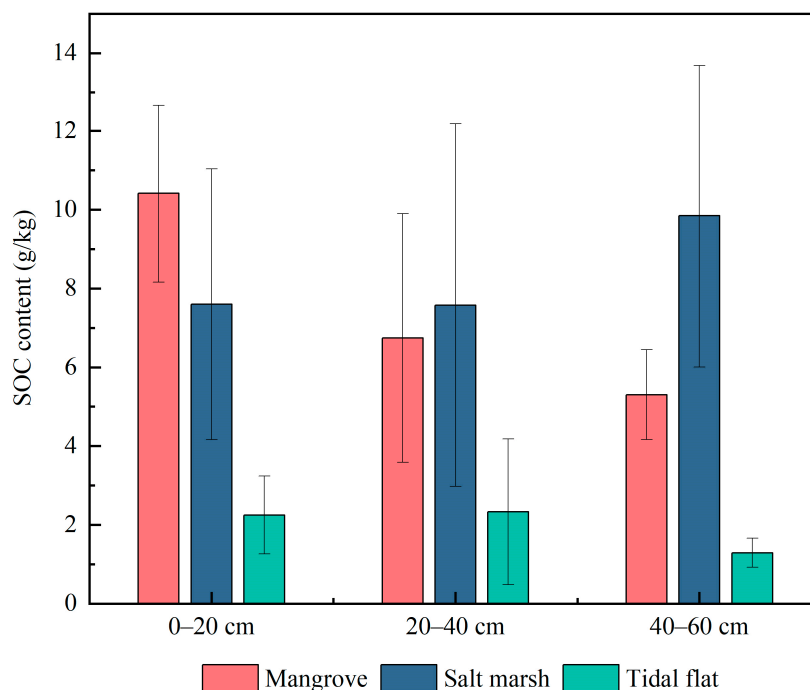


Figure 11. The SOC Content in Different Habitats at Various Soil Depths (0–20 cm, 20–40 cm, 40–60 cm).

As shown in Figure 12, in the surface soil layer (0–20 cm), the SOCS of each habitat type were ranked as follows: mangroves > salt marsh > tidal flats. The SOCS of mangroves reach their maximum value in this soil layer, being 3.86 times that of tidal flats and 1.35 times that of salt marshes. Meanwhile, the SOCS of salt marshes are 2.85 times that of tidal flats. As the soil depth increases to 20–40 cm, the difference in SOCS between mangroves and salt marshes remains minimal, staying at approximately 2.65 and 2.83 times that of tidal flats, respectively. However, at a depth of 40–60 cm, the SOCS of salt marshes exhibit a significant increase, reaching 6.70 times that of tidal flats, while mangroves are only 3.44 times that of tidal flats. These findings indicated that both mangroves and salt marshes demonstrate considerable carbon sequestration capabilities, with mangroves exhibiting the strongest capacity in surface soil layers, while salt marshes excel in deeper soil layers.

Through the correlation analysis between SOC, SOCS, and soil physicochemical factors (see Table 9), it was observed that soil physicochemical factors have an impact on SOC and SOCS. Compared to inland wetlands, forests, and agricultural fields, tidal wetlands are characterized by longer periods of waterlogging, higher MC, and prolonged anaerobic conditions. This inhibits the activity of aerobic microorganisms, reduces SOC consumption, and promotes SOC accumulation. As shown in Table 8, soils in mangroves and salt marshes are weakly acidic, while those in tidal flats are weakly alkaline. Research has indicated that soil pH can affect the growth, quantity, and activity of microorganisms [64]. In acidic soils, microbial diversity is limited, with fungi dominating, which slows down the turnover rate of labile organic carbon fractions and promotes SOC accumulation [65]. BD represents soil compaction and is one of the parameters for calculating SOCS. From Table 9, it is evident that SOC and SOCS are negatively correlated with BD. This is mainly because BD affects soil porosity, with higher bulk densities usually associated with lower soil porosity, which is unfavorable for organic matter accumulation [66]. In this study, at a depth of 0–20 cm, mangroves have lower BD compared to salt marshes and tidal flats, higher MC than both, and acidic soil conditions, resulting in higher SOC and SOCS than salt marshes and tidal flats, demonstrating that soil physicochemical factors influence SOC and SOCS.

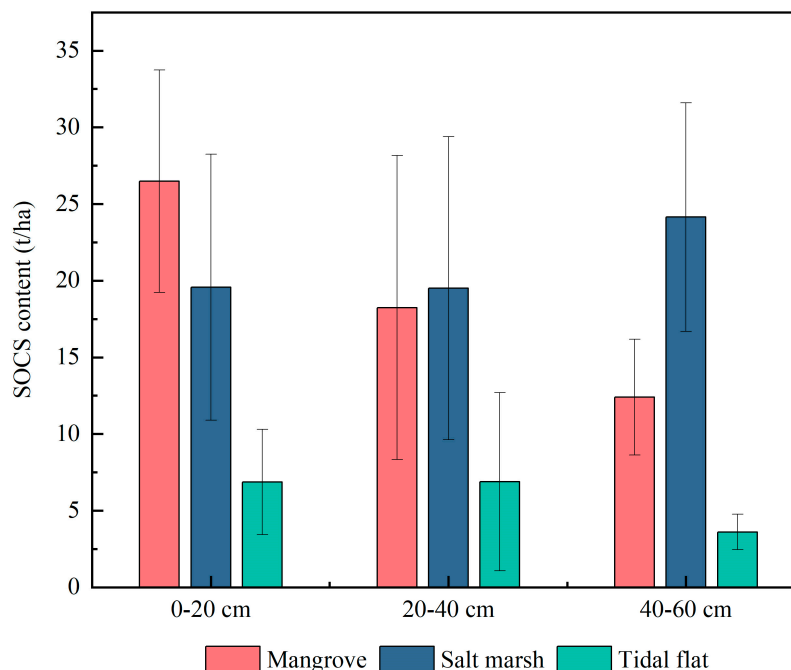


Figure 12. The SOCS Content in Different Habitats at Various Soil Depths (0–20 cm, 20–40 cm, 40–60 cm).

5. Conclusions

In previous studies, many global wetland data and regional wetland data have been published. For example, Zhang et al. [49] generated the world's first 30 m wetland product in 2020; the East Asian tidal wetland data with 10 m resolution in 2020 generated by Zhang et al. [51], but there is still a lack of continuous 10 m tidal wetland dataset for the coastal zone of Guangxi. Therefore, by integrating the existing tidal wetland data, based on the Sentinel-2 L2 A time series images, combined with the random forest algorithm, this study generated a 10 m tidal wetland dataset in Guangxi from 2019 to 2023, including mangroves, salt marshes and tidal flats. Subsequently, based on the classification results of tidal wetlands in 2023, the method of time instead of space was used to explore the changes of soil organic carbon and soil organic carbon storage under different habitat categories of tidal wetlands.

The results showed that the overall accuracy of tidal wetland identification in Guangxi from 2019 to 2023 was higher than 96%, and the Kappa coefficient was higher than 0.95, indicating that the identification results had high accuracy. Compared with other tidal wetland data, the phenomena of misrecognition and missed recognition are reduced, which proves that the research method is suitable for the identification of tidal wetlands in complex landform areas. Quantitative statistical analysis shows that in Guangxi's tidal wetlands, tidal flats account for about 80% of the total area, mangroves account for about 15%, and salt marshes account for less than 10% of the total area. Additionally, experimental results indicated that in the surface layer (0–20 cm) of soil, soil organic carbon and soil organic carbon storage were ranked in the following order across habitat types: mangroves > salt marshes > tidal flats. Whereas at depths of 20–40 cm and 40–60 cm, soil organic carbon and soil organic carbon storage were ranked as follows: salt marshes > mangroves > tidal flats. The study results also suggested that certain soil physicochemical factors, such as bulk density, moisture content, and pH, were among the driving factors influencing soil organic carbon and soil organic carbon storage in tidal wetlands.

However, there are still many uncertainties and limitations in the proposed wetland identification methods and identification results. In the process of generating stable sample points, the collected tidal wetland datasets are current up to 2020, and after that, the wetland category may change, which may lead to a certain proportion of errors in the sample points automatically generated based on the existing datasets. Therefore, it is necessary to further collect multi-source datasets to fill these gaps and improve the accuracy and comprehensiveness of wetland identification. In addition, in this study, only four carbon components of soil organic carbon, dissolved organic carbon, easily oxidized organic carbon and particulate organic carbon, were explored. Other carbon components in the soil were not analyzed and studied, such as mineral-associated organic carbon, microbial biomass carbon, etc. In the future, it is necessary to further study the soil carbon components and soil carbon pool composition of tidal wetlands in Dandou Sea area of Guangxi. This is conducive to a more comprehensive understanding of the carbon storage and cycle processes of wetland ecosystems, and provides a scientific basis for wetland protection and sustainable development.

Author Contributions: Conceptualization, H.Y.; methodology, M.W.; software, M.W.; validation, Y.L., M.C., M.Z. and J.Q.; formal analysis, Z.H.; writing—original draft preparation, M.W. All authors have read and agreed to the published version of the manuscript.

Funding: This research received no external funding.

Institutional Review Board Statement: Not applicable.

Informed Consent Statement: Not applicable.

Data Availability Statement: The Sentinel-2 image and AW3D_30 data can be obtained from the Google Earth Engine (GEE) platform (<https://earthengine.google.com/>, accessed on 20 September 2023). WAM, GWM v3.0, GBTM, GDM_USGS and Global distribution of tidal flat wetland ecosystems are available from the Ocean Data Viewer (<https://data.unep-wcmc.org/datasets/45>, accessed on 23 October 2023). GMCP can be acquired from the Science Data Bank (<https://www.scidb.cn/>, accessed on 23 October 2023), and Spatial distribution of *Spartina alterniflora* in China can be acquired from the National Earth System Science Data Center (<https://www.geodata.cn/>, accessed on 23 October 2023).

Acknowledgments: Acknowledgement for the data support from “National Earth System Science Data Center. (<https://www.geodata.cn/>)”, “Ocean Data Viewer. (<https://data.unep-wcmc.org/>)”, and “Science Data Bank. (<https://www.scidb.cn/>)”.

Conflicts of Interest: The authors declare no conflicts of interest.

Appendix A

Table A1. List of Abbreviations.

Abbreviation	Definition
BD	Bulk density
EC	Electrical conductivity
EOC	Easily oxidizable organic carbon
EVI	Enhanced Vegetation Index
GEE	Google Earth Engine
LSWI	Land Surface Water Index
MC	Moisture content
mNDWI	Modified Normalized Difference Water Index
MVI	Mangrove Vegetation Index
NDVI	Normalized Difference Vegetation Index
NDWI	Normalized Water Difference Index

Table A1. Cont.

Abbreviation	Definition
NIR	Near-infrared
PA	Producer accuracy
POC	Particulate organic carbon
RF	Random forest
<i>S. alterniflora</i>	<i>Spartina alterniflora</i>
SOC	Soil organic carbon
SOCS	Soil organic carbon stock
SWIR1	Shortwave infrared band 1
UA	User accuracy

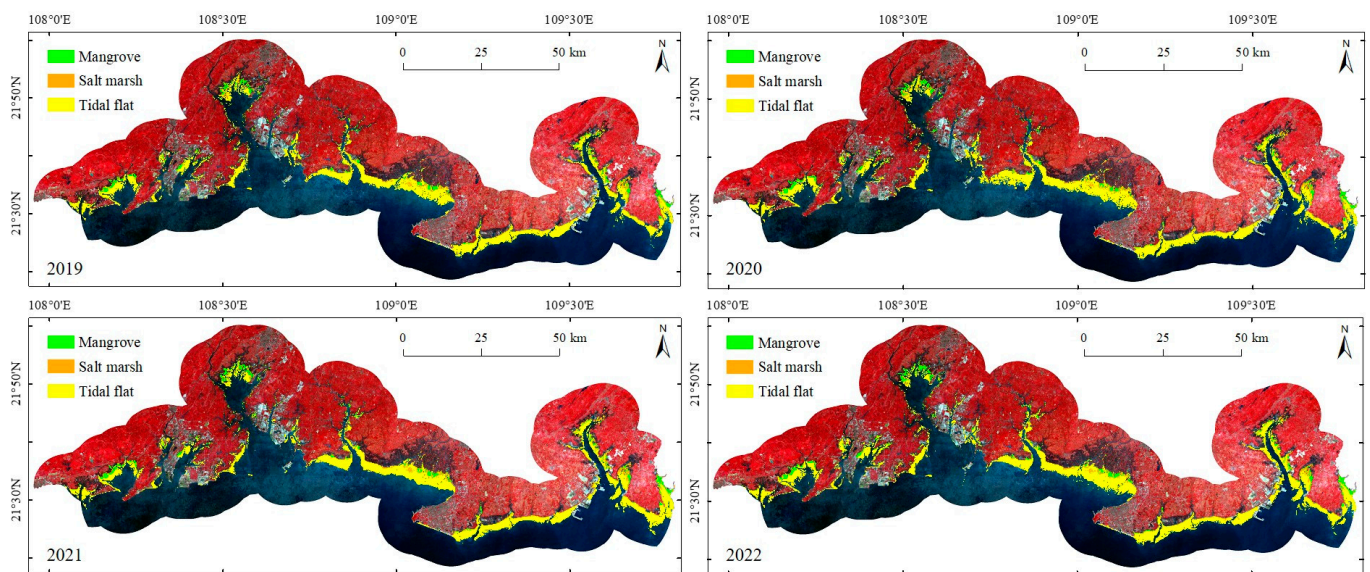


Figure A1. Spatial Distribution of Tidal Wetlands from 2019 to 2022(In the base map, the Sentinel-2 satellite image is displayed as a false-color composite, with black areas representing water and red areas indicating vegetation).

Table A2. Nomenclature.

Mathematical Symbol	Meaning	Source of Mathematical Symbols
BD_i	The soil BD in i soil depth (g/cm^3)	Formula (12)
C_i	Carbon mass fraction in i soil depth (g/kg)	Formula (12)
China <i>S. alterniflora</i>	Spatial distribution of <i>S. alterniflora</i> in China data	Formula (2)
DW	The soil dry weight	Formula (10)
E_i	Thickness of soil in i soil depth (cm)	Formula (12)
FW	The soil fresh weight	Formula (10)
g	The fresh weight of ring knife soil (g)	Formula (11)
Guangxi <i>S. alterniflora</i> _{t}	The distribution data of <i>S. alterniflora</i> in Guangxi for year, t	Formula (2)
Line _{coastal} 10 km	A 10 km buffer zone towards the sea	Formula (3)
MaxExtent _{Mangrove}	The maximum extent of mangrove	Formula (1)
MaxExtent _{salt marsh}	The maximum extent of salt marsh	Formula (2)
MaxExtent _{Tidal flat}	The maximum extent of tidal flat	Formula (3)

Table A2. *Cont.*

Mathematical Symbol	Meaning	Source of Mathematical Symbols
M_{GBTM}	A global biophysical typology of mangroves data	
M_{GDM_USGS}	Global distribution of mangroves USGS	
M_{GMCP}	Global Mangrove Classification Products data	Formula (1)
M_{GMW}	Global Mangrove Watch data	
M_{WAM}	World Atlas of Mangroves data	
n	The number of soil depth layers	Formula (12)
Tidal flat _t	The global tidal wetland ecosystem distribution data for year, t	Formula (3)
v	The ring knife volume (100 cm ³)	Formula (11)
ρ_{Blue}	The blue band in the Sentinel-2 images	Formula (8)
ρ_{Green}	The green band in the Sentinel-2 images	Formulas (5), (6) and (9)
ρ_{Red}	The red band in the Sentinel-2 images	Formulas (4) and (8)
ρ_{NIR}	The near-infrared band in the Sentinel-2 images	Formulas (4), (5) and (7)–(9)
ρ_{SWIR1}	The shortwave infrared band 1 in the Sentinel-2 images	Formulas (6), (7) and (9)

Table A3. Confusion Matrix for “Mangroves”, “Salt Marshes”, “Intertidal Flats”, and “Other” Categories in 2019.

Type	Mangrove	Salt Marsh	Tidal Flat	Other	PA
Mangrove	277	1	0	0	0.987
Salt marsh	0	204	4	5	0.958
Tidal flat	0	6	231	10	0.935
Other	2	0	4	393	0.985
UA	0.991	0.976	0.947	0.958	

Table A4. Confusion Matrix for “Mangroves”, “Saltmarshes”, “Intertidal Flats”, and “Other” Categories in 2020.

Type	Mangrove	Salt Marsh	Tidal Flat	Other	PA
Mangrove	239	0	0	0	1
Salt marsh	1	230	4	2	0.970
Tidal flat	0	4	261	1	0.981
Other	1	1	2	425	0.991
UA	0.992	0.979	0.978	0.993	

Table A5. Confusion Matrix for “Mangroves”, “Salt Marshes”, “Intertidal Flats”, and “Other” Categories in 2021.

Type	Mangrove	Salt Marsh	Tidal Flat	Other	PA
Mangrove	237	2	1	0	0.988
Salt marsh	0	228	2	3	0.979
Tidal flat	0	7	227	5	0.950
Other	0	0	5	437	
UA	0.988	0.970	0.974	0.975	

Table A6. Confusion Matrix for “Mangroves”, “Salt Marshes”, “Intertidal Flats”, and “Other” Categories in 2022.

Type	Mangrove	Salt Marsh	Tidal Flat	Other	PA
Mangrove	216	0	0	1	0.991
Salt marsh	2	244	6	8	0.938
Tidal flat	0	10	219	3	0.961
Other	1	2	11	414	0.965
UA	0.986	0.953	0.928	0.972	

Table A7. Confusion Matrix for “Mangroves”, “Salt Marshes”, “Intertidal Flats”, and “Other” Categories in 2023.

Type	Mangrove	Salt Marsh	Tidal Flat	Other	PA
Mangrove	240	0	0	0	1
Salt marsh	0	224	5	0	0.961
Tidal flat	0	0	220	2	0.991
Other	0	0	2	444	0.995
UA	1	1	0.969	0.987	

Table A8. Correlation between SOC and its Active Components in Mangrove Soils and Other Physicochemical Properties of Soil.

	BD	MC	pH	EC	SOC	SOCS	EOC	POC	DOC
BD	1								
MC	−0.990 **	1							
pH	−0.726 *	0.816 **	1						
EC	0.246	−0.107	0.488	1					
SOC	0.399	−0.265	0.342	0.987 **	1				
SOCS	0.577 *	−0.456	0.143	0.934 **	0.979 **	1			
EOC	0.016	0.126	0.676 *	0.973 **	0.923 **	0.826 **	1		
POC	0.547 *	−0.424	0.178	0.946 **	0.986 **	0.999 **	0.845 **	1	
DOC	0.958 **	−0.989 **	−0.893 **	−0.043	0.118	0.318	−0.272	0.284	1

** $p < 0.01$, * $p < 0.05$.

Table A9. Correlation between SOC and its Active Components in Salt marsh Soils and Other Physicochemical Properties of Soil.

	BD	MC	pH	EC	SOC	SOCS	EOC	POC	DOC
BD	1								
MC	−0.808 **	1							
pH	−0.104	−0.502 *	1						
EC	−0.570 *	0.945 **	−0.757 *	1					
SOC	−0.591 *	0.953 **	−0.740 *	1.000 **	1				
SOCS	−0.596 *	0.955 **	−0.736 *	1.000 **	1.000 **	1			
EOC	−0.176	0.722 *	−0.961 **	0.909 **	0.898 **	0.895 **	1		
POC	−0.667 *	0.978 **	−0.672 *	0.992 **	0.995 **	0.996 **	0.851 **	1	
DOC	−0.999 **	0.839 **	0.050 *	0.614 *	0.635 *	0.639 *	0.229	0.706 *	1

** $p < 0.01$, * $p < 0.05$.

Table A10. Correlation between SOC and its Active Components in Tidal flat Soils and Other Physicochemical Properties of Soil.

	BD	MC	pH	EC	SOC	SOCS	EOC	POC	DOC
BD	1								
MC	−0.959 **	1							
pH	0.672 *	−0.435	1						
EC	−0.377	0.623 *	0.433	1					
SOC	0.965 **	−1.000 **	0.455	−0.606 *	1				
SOCS	0.947 **	−0.999 **	0.400	−0.653 *	0.998 **	1			
EOC	0.867 **	−0.691 *	0.952 **	0.135	0.707 *	0.662 *	1		
POC	0.934 **	−0.795 *	0.892 **	−0.021	0.808 **	0.771 *	0.988 **	1	
DOC	0.929 **	−0.786 *	0.899 **	−0.006	0.799 *	0.761 *	0.990 **	1.000 **	1

** $p < 0.01$, * $p < 0.05$.

References

- Luo, Y.; Li, Y.; Zhang, H. *Soil and Environment in Yellow River Delta*, 1st ed.; Science Press: Beijing, China, 2017; p. 5.
- Guo, J.; Ma, Y.; Ding, C.; Zhao, H.; Cheng, Z.; Yan, G.; You, Z. Impacts of Tidal Oscillations on Coastal Groundwater System in Reclaimed Land. *J. Mar. Sci. Eng.* **2023**, *11*, 2019. [\[CrossRef\]](#)
- Wang, X.; Zhang, H.; Han, G. Carbon Cycle and “Blue Carbon” Potential in China’s Coastal Zone. *Bull. Chin. Acad. Sci.* **2016**, *31*, 1218–1225. [\[CrossRef\]](#)
- Wang, R.; Zhang, M.; Wu, H.; Li, Y. Analysis on Wetland Definition and Classification of the Wetland Conservation Law of the People’s Republic of China. *Wetl. Sci.* **2022**, *20*, 404–412. [\[CrossRef\]](#)
- UNEP-WCMC; UNEP; IUCN. *Protected Planet Report 2020*; United Nations Environment Programme: Nairobi, Kenya, 2021.
- Ma, K.; Zhang, Y.; Tang, S.; Liu, J. Spatial Distribution of Soil Organic Carbon in the Zoige Alpine Wetland, Northeastern Qinghai–Tibet Plateau. *Catena* **2016**, *144*, 102–108. [\[CrossRef\]](#)
- Lehner, B.; Döll, P. Development and Validation of a Global Database of Lakes, Reservoirs and Wetlands. *J. Hydrol.* **2004**, *296*, 1–22. [\[CrossRef\]](#)
- Erwin, K.L. Wetlands and Global Climate Change: The Role of Wetland Restoration in a Changing World. *Wetl. Ecol. Manag.* **2009**, *17*, 71–84. [\[CrossRef\]](#)
- Lehmann, J. A Handful of Carbon. *Nature* **2007**, *447*, 143–144. [\[CrossRef\]](#)
- Kirwan, M.L.; Blum, L.K. Enhanced Decomposition Offsets Enhanced Productivity and Soil Carbon Accumulation in Coastal Wetlands Responding to Climate Change. *Biogeosciences* **2011**, *8*, 987–993. [\[CrossRef\]](#)
- Cao, Q.; Wang, R.; Zhang, H.; Ge, X.; Liu, J. Distribution of Organic Carbon in the Sediments of Xinxue River and the Xinxue River Constructed Wetland, China. *PLoS ONE* **2015**, *10*, e0134713. [\[CrossRef\]](#)
- Lehmann, J.; Kleber, M. The Contentious Nature of Soil Organic Matter. *Nature* **2015**, *528*, 60–68. [\[CrossRef\]](#)
- Luo, Z.; Feng, W.; Luo, Y.; Baldock, J.; Wang, E. Soil Organic Carbon Dynamics Jointly Controlled by Climate, Carbon Inputs, Soil Properties and Soil Carbon Fractions. *Glob. Chang. Biol.* **2017**, *23*, 4430–4439. [\[CrossRef\]](#)
- Zhao, H.; Jia, J.; Zhao, Q.; Wang, J.; Gao, Y.; Huang, Y.; Chen, G. Soil Organic Carbon Stabilization and Associated Mineral Protection in Typical Coastal Wetlands under Different Hydrologic Conditions. *Front. Mar. Sci.* **2022**, *9*, 1031561. [\[CrossRef\]](#)
- Averill, C.; Turner, B.L.; Finzi, A.C. Mycorrhiza-Mediated Competition between Plants and Decomposers Drives Soil Carbon Storage. *Nature* **2014**, *505*, 543–545. [\[CrossRef\]](#)
- Jobbágy, E.G.; Jackson, R.B. The Vertical Distribution of Soil Organic Carbon and its Relation to Climate and Vegetation. *Ecol. Appl.* **2000**, *10*, 423–436. [\[CrossRef\]](#)
- Lal, R. Soil Carbon Sequestration Impacts on Global Climate Change and Food Security. *Science* **2004**, *304*, 1623–1627. [\[CrossRef\]](#)
- Ji, H.; Han, J.; Xue, J.; Hatten, J.A.; Wang, M.; Guo, Y.; Li, P. Soil Organic Carbon Pool and Chemical Composition under Different Types of Land Use in Wetland: Implication for Carbon Sequestration in Wetlands. *Sci. Total Environ.* **2020**, *716*, 136996. [\[CrossRef\]](#)
- Vaughn, D.R.; Bianchi, T.S.; Shields, M.R.; Kenney, W.F.; Osborne, T.Z. Increased Organic Carbon Burial in Northern Florida Mangrove-Salt Marsh Transition Zones. *Glob. Biogeochem. Cycles* **2020**, *34*, e2019GB006334. [\[CrossRef\]](#)
- Weiss, C.; Weiss, J.; Boy, J.; Iskandar, I.; Mikutta, R.; Guggenberger, G. Soil Organic Carbon Stocks in Estuarine and Marine Mangrove Ecosystems Are Driven by Nutrient Colimitation of P and N. *Ecol. Evol.* **2016**, *6*, 5043–5056. [\[CrossRef\]](#)
- De Jong Cleyndert, G.; Cuni-Sanchez, A.; Seki, H.A.; Shirima, D.D.; Munishi, P.K.T.; Burgess, N.; Calders, K.; Marchant, R. The Effects of Seaward Distance on above and below Ground Carbon Stocks in Estuarine Mangrove Ecosystems. *Carbon Balance Manag.* **2020**, *15*, 27. [\[CrossRef\]](#)
- Kauffman, J.B.; Heider, C.; Cole, T.G.; Dwire, K.A.; Donato, D.C. Ecosystem Carbon Stocks of Micronesian Mangrove Forests. *Wetlands* **2011**, *31*, 343–352. [\[CrossRef\]](#)
- Donato, D.C.; Kauffman, J.B.; Murdiyarso, D.; Kurnianto, S.; Stidham, M.; Kanninen, M. Mangroves among the Most Carbon-Rich Forests in the Tropics. *Nat. Geosci.* **2011**, *4*, 293–297. [\[CrossRef\]](#)

24. Kida, M.; Tomotsune, M.; Iimura, Y.; Kinjo, K.; Ohtsuka, T.; Fujitake, N. High Salinity Leads to Accumulation of Soil Organic Carbon in Mangrove Soil. *Chemosphere* **2017**, *177*, 51–55. [[CrossRef](#)]
25. Sun, H.; Jiang, J.; Cui, L.; Feng, W.; Wang, Y.; Zhang, J. Soil Organic Carbon Stabilization Mechanisms in a Subtropical Mangrove and Salt Marsh Ecosystems. *Sci. Total Environ.* **2019**, *673*, 502–510. [[CrossRef](#)]
26. Wang, F.; Guo, R.; Zhang, N.; Yang, S.; Cao, W. Soil Organic Carbon Storages and Bacterial Communities along a Restored Mangrove Soil Chronosequence in the Jiulong River Estuary: From Tidal Flats to Mangrove Afforestation. *Fundam. Res.* **2023**, *3*, 880–889. [[CrossRef](#)]
27. Eid, E.M.; Arshad, M.; Shaltout, K.H.; El-Sheikh, M.A.; Alfarhan, A.H.; Picó, Y.; Barcelo, D. Effect of the Conversion of Mangroves into Shrimp Farms on Carbon Stock in the Sediment along the Southern Red Sea Coast, Saudi Arabia. *Environ. Res.* **2019**, *176*, 108536. [[CrossRef](#)]
28. Wang, Q.; Wen, Y.; Zhao, B.; Hong, H.; Liao, R.; Li, J.; Liu, J.; Lu, H.; Yan, C. Coastal Soil Texture Controls Soil Organic Carbon Distribution and Storage of Mangroves in China. *Catena* **2021**, *207*, 105709. [[CrossRef](#)]
29. Zhu, Z.; Wang, S.; Woodcock, C.E. Improvement and Expansion of the Fmask Algorithm: Cloud, Cloud Shadow, and Snow Detection for Landsats 4–7, 8, and Sentinel 2 Images. *Remote Sens. Environ.* **2015**, *159*, 269–277. [[CrossRef](#)]
30. Takaku, J.; Tadono, T.; Tsutsui, K. Generation of High Resolution Global DSM from ALOS PRISM. *Int. Arch. Photogramm. Remote Sens. Spat. Inf. Sci.* **2014**, *40*, 243–248. [[CrossRef](#)]
31. Tadono, T.; Ishida, H.; Oda, F.; Naito, S.; Minakawa, K.; Iwamoto, H. Precise Global DEM Generation by ALOS PRISM. *ISPRS Ann. Photogramm. Remote Sens. Spatial Inf. Sci.* **2014**, *2*, 71–76. [[CrossRef](#)]
32. Tadono, T.; Nagai, H.; Ishida, H.; Oda, F.; Naito, S.; Minakawa, K.; Iwamoto, H. Generation of the 30 m-mesh Global Digital Surface Model by ALOS PRISM. *Int. Arch. Photogramm. Remote Sens. Spatial Inf. Sci.* **2016**, *41*, 157–162. [[CrossRef](#)]
33. Murray, N.J.; Worthington, T.A.; Bunting, P.; Duce, S.; Hagger, V.; Lovelock, C.E.; Lucas, R.; Saunders, M.I.; Sheaves, M.; Spalding, M.; et al. High-Resolution Mapping of Losses and Gains of Earth’s Tidal Wetlands. *Science* **2022**, *376*, 744–749. [[CrossRef](#)]
34. Bunting, P.; Rosenqvist, A.; Hilarides, L.; Lucas, R.M.; Thomas, N.; Tadono, T.; Worthington, T.A.; Spalding, M.; Murray, N.J.; Rebelo, L.-M. Global Mangrove Extent Change 1996–2020: Global Mangrove Watch Version 3.0. *Remote Sens.* **2022**, *14*, 3657. [[CrossRef](#)]
35. Zhang, X.; Liu, L.; Chen, X.; Gao, Y.; Xie, S.; Mi, J. GLC_FCS30: Global Land-Cover Product with Fine Classification System at 30 m Using Time-Series Landsat Imagery. *Earth Syst. Sci. Data* **2021**, *13*, 2753–2776. [[CrossRef](#)]
36. Chen, J.; Chen, J.; Liao, A.; Cao, X.; Chen, L.; Chen, X.; He, C.; Han, G.; Peng, S.; Lu, M.; et al. Global Land Cover Mapping at 30m Resolution: A POK-Based Operational Approach. *ISPRS J. Photogramm. Remote Sens.* **2015**, *103*, 7–27. [[CrossRef](#)]
37. Spalding, M. *World Atlas of Mangroves*; Routledge, A Collaborative Project of ITTO, ISME, FAO, UNEP-WCMC, UNESCO-MAB, UNU-INWEH and TNC; Earthscan: London, UK, 2010. [[CrossRef](#)]
38. Worthington, T.A.; Zu Ermgassen, P.S.E.; Friess, D.A.; Krauss, K.W.; Lovelock, C.E.; Thorley, J.; Tingey, R.; Woodroffe, C.D.; Bunting, P.; Cormier, N.; et al. A Global Biophysical Typology of Mangroves and Its Relevance for Ecosystem Structure and Deforestation. *Sci. Rep.* **2020**, *10*, 14652. [[CrossRef](#)]
39. Xiao, H.; Su, F.; Fu, D.; Yu, H.; Ju, C.; Pan, T.; Kang, L. 10-m Global Mangrove Classification Products of 2018–2020 Based on Big Data. V1. *Sci. Data Bank* **2021**. [[CrossRef](#)]
40. Giri, C.; Ochieng, E.; Tieszen, L.L.; Zhu, Z.; Singh, A.; Loveland, T.; Masek, J.; Duke, N. Status and Distribution of Mangrove Forests of the World Using Earth Observation Satellite Data. *Glob. Ecol. Biogeogr.* **2011**, *20*, 154–159. [[CrossRef](#)]
41. Mao, D.; Wang, Z.; Du, B.; Li, L.; Tian, Y.; Jia, M.; Zeng, Y.; Song, K.; Jiang, M.; Wang, Y. National Wetland Mapping in China: A New Product Resulting from Object-Based and Hierarchical Classification of Landsat 8 OLI Images. *ISPRS J. Photogramm. Remote Sens.* **2020**, *164*, 11–25. [[CrossRef](#)]
42. Mao, D.; Liu, M.; Wang, Z.; Li, L.; Man, W.; Jia, M.; Zhang, Y. Rapid Invasion of *Spartina Alterniflora* in the Coastal Zone of Mainland China: Spatiotemporal Patterns and Human Prevention. *Sensors* **2019**, *19*, 2308. [[CrossRef](#)]
43. Liu, M.; Mao, D.; Wang, Z.; Li, L.; Man, W.; Jia, M.; Ren, C.; Zhang, Y. Rapid Invasion of *Spartina Alterniflora* in the Coastal Zone of Mainland China: New Observations from Landsat OLI Images. *Remote Sens.* **2018**, *10*, 1933. [[CrossRef](#)]
44. Huang, Y. Remote Sensing Monitoring and Driving Factors of *Spartina Alterniflora* Invasion in Guangxi Coastal Zone. Master’s Thesis, Guangxi University, Nanning, China, 2022.
45. Lu, Y.; Dai, L.; Yan, G.; Huo, Z.; Chen, W.; Lan, J.; Zhang, C.; Xu, Q.; Deng, S.; Chen, J. Effects of Various Land Utilization Types on Groundwater at Different Temporal Scales: A Case Study of Huocheng Plain, Xinjiang, China. *Front. Environ. Sci.* **2023**, *11*, 1225916. [[CrossRef](#)]
46. Tucker, C.J. Red and Photographic Infrared Linear Combinations for Monitoring Vegetation. *Remote Sens. Environ.* **1979**, *8*, 127–150. [[CrossRef](#)]
47. Xu, H. Modification of Normalised Difference Water Index (NDWI) to Enhance Open Water Features in Remotely Sensed Imagery. *Int. J. Remote Sens.* **2006**, *27*, 3025–3033. [[CrossRef](#)]
48. Gao, B. NDWI—A Normalized Difference Water Index for Remote Sensing of Vegetation Liquid Water from Space. *Remote Sens. Environ.* **1996**, *58*, 257–266. [[CrossRef](#)]
49. Zhang, X.; Liu, L.; Zhao, T.; Chen, X.; Lin, S.; Wang, J.; Mi, J.; Liu, W. GWL_FCS30: A Global 30 m Wetland Map with a Fine Classification System Using Multi-Sourced and Time-Series Remote Sensing Imagery in 2020. *Earth Syst. Sci. Data* **2023**, *15*, 265–293. [[CrossRef](#)]

50. Baloloy, A.B.; Blanco, A.C.; Ana, R.R.C.S.; Nadaoka, K. Development and Application of a New Mangrove Vegetation Index (MVI) for Rapid and Accurate Mangrove Mapping. *ISPRS J. Photogramm. Remote Sens.* **2020**, *166*, 95–117. [[CrossRef](#)]
51. Zhang, Z.; Xu, N.; Li, Y.; Li, Y. Sub-Continental-Scale Mapping of Tidal Wetland Composition for East Asia: A Novel Algorithm Integrating Satellite Tide-Level and Phenological Features. *Remote Sens. Environ.* **2022**, *269*, 112799. [[CrossRef](#)]
52. Ludwig, C.; Walli, A.; Schleicher, C.; Weichselbaum, J.; Riffler, M. A Highly Automated Algorithm for Wetland Detection Using Multi-Temporal Optical Satellite Data. *Remote Sens. Environ.* **2019**, *224*, 333–351. [[CrossRef](#)]
53. Li, Z.; Chen, H.; White, J.C.; Wulder, M.A.; Hermosilla, T. Discriminating Treed and Non-Treed Wetlands in Boreal Ecosystems Using Time Series Sentinel-1 Data. *Int. J. Appl. Earth Obs. Geoinf.* **2020**, *85*, 102007. [[CrossRef](#)]
54. Zhang, X.; Liu, L.; Chen, X.; Gao, Y.; Jiang, M. Automatically Monitoring Impervious Surfaces Using Spectral Generalization and Time Series Landsat Imagery from 1985 to 2020 in the Yangtze River Delta. *J. Remote Sens.* **2021**, *2021*, 9873816. [[CrossRef](#)]
55. Hansen, M.C.; Egorov, A.; Potapov, P.V.; Stehman, S.V.; Tyukavina, A.; Turubanova, S.A.; Roy, D.P.; Goetz, S.J.; Loveland, T.R.; Ju, J.; et al. Monitoring Conterminous United States (CONUS) Land Cover Change with Web-Enabled Landsat Data (WELD). *Remote Sens. Environ.* **2014**, *140*, 466–484. [[CrossRef](#)]
56. Zhang, H.K.; Roy, D.P. Using the 500 m MODIS Land Cover Product to Derive a Consistent Continental Scale 30 m Landsat Land Cover Classification. *Remote Sens. Environ.* **2017**, *197*, 15–34. [[CrossRef](#)]
57. Azzari, G.; Lobell, D.B. Landsat-Based Classification in the Cloud: An Opportunity for a Paradigm Shift in Land Cover Monitoring. *Remote Sens. Environ.* **2017**, *202*, 64–74. [[CrossRef](#)]
58. Ng, W.-T.; Rima, P.; Einzmann, K.; Immitzer, M.; Atzberger, C.; Eckert, S. Assessing the Potential of Sentinel-2 and Pléiades Data for the Detection of *Prosopis* and *Vachellia* Spp. in Kenya. *Remote Sens.* **2017**, *9*, 74. [[CrossRef](#)]
59. Bunting, P.; Rosenqvist, A.; Hilarides, L.; Lucas, R.M.; Thomas, N. Global Mangrove Watch: Updated 2010 Mangrove Forest Extent (v2.5). *Remote Sens.* **2022**, *14*, 1034. [[CrossRef](#)]
60. Zhang, J. Study on Vegetation Succession and Soil Organic Carbon Distribution in Yancheng Coastal Wetland. Master's Thesis, Nanjing Normal University, Nanjing, China, 2019.
61. Arunrat, N.; Sansupa, C.; Kongsurakan, P.; Sereenonchai, S.; Hatano, R. Soil Microbial Diversity and Community Composition in Rice–Fish Co-Culture and Rice Monoculture Farming System. *Biology* **2022**, *11*, 1242. [[CrossRef](#)] [[PubMed](#)]
62. Chu, M.; Xiao, X.; Ding, Y.; Zhao, M. Sediment Organic Matter and Carbon Stock Associated with a Mangrove Reserve in Danzhou Bay, Hainan, China. *Mar. Sci.* **2021**, *45*, 22–31.
63. Xiao, Y.; Huang, Z.; Wu, H.; Lu, X. Compositions and Contents of Active Organic Carbon in Different Wetland Soils in Sanjiang Plain, Northeast China. *Acta Ecol. Sin.* **2015**, *35*, 7625–7633. [[CrossRef](#)]
64. Arunrat, N.; Sansupa, C.; Sereenonchai, S.; Hatano, R. Short-Term Response of Soil Bacterial and Fungal Communities to Fire in Rotational Shifting Cultivation, Northern Thailand. *Appl. Soil Ecol.* **2024**, *196*, 105303. [[CrossRef](#)]
65. Xu, W.; Qiao, M. Soil Carbon Contents in Relation to Soil Physicochemical Properties in Arid Regions of China. *J. Desert Res.* **2014**, *34*, 1558–1561. [[CrossRef](#)]
66. Zhou, C.; Ma, H. Distribution of Labile Organic Carbon in Soil as Affected by Vegetation Typical of Sygera Mountains, Tibet, China. *Acta Pedol. Sin.* **2013**, *50*, 1246–1251. [[CrossRef](#)]

Disclaimer/Publisher's Note: The statements, opinions and data contained in all publications are solely those of the individual author(s) and contributor(s) and not of MDPI and/or the editor(s). MDPI and/or the editor(s) disclaim responsibility for any injury to people or property resulting from any ideas, methods, instructions or products referred to in the content.